Cone-Beam Computed Tomography: Imaging Dose during CBCT Scan Acquisition and Accuracy of CBCT Based Dose Calculations

David Matthew Giles

Medical Physics Unit

McGill University

Montreal, QC, Canada

May, 2010

A thesis submitted to the Faculty of Graduate Studies and Research in partial fulfillment of the requirements of the degree of Master of Sciences in Medical Radiation Physics

Dedication

This thesis is dedicated to my wife Kacy and to my daughters Mary Beth and Emalyn.

Acknowledgements

First I would like to thank my supervisor Nada Tomic for all the time and effort she gave to seeing me through this project. Her expertise in cone beam computed tomography was invaluable and her insight spurred my understanding of the subject. The hospitality that she and her family showed to me during my stay in Montreal is a memory I am glad to take with me.

I would also like to thank my local supervisor Dr. Peter Mondalek for his guidance and his patience, as well as for the use of the facilities of ROSA and AOA which made much of my work possible.

I am thankful to David Quarin for the VBA scripts he wrote which were invaluable in my data analysis.

I am indebted to Dr. Slobodan Devic for his time and for the use of his MatLab scripting in my work. Our conversations were always fruitful and left me with much to think about.

I would like to thank François DeBlois for his work as co-supervisor to me during my research.

Dr. Genevieve Jarry allowed me to use her equipment in my research and spent a long Sunday helping me take measurements. For this I am grateful.

I would like to thank Dr. Jan Seuntjens for his guidance in selecting a thesis topic and for the flexibility he gave me which allowed me to continue to study medical physics.

Lisette Smith and Ernesto Gutierrez gave their time to teach me treatment planning which I truly appreciate.

I would like to thank Eric Elder for loaning me his anthropomorphic phantom for this project.

I am thankful for the education in physics I received from the faculty and staff of the Medical Physics Unit, which laid the foundation for this endeavour and for my future development as a physicist. In particular I would like to acknowledge Dr. Podgorsak whose unyielding standard was a driving force in my studies. Also I am grateful to Margery Knewstubb, the department secretary for keeping me up to date with all that went on.

I would like to thank my mom for always expecting the best of me and accepting nothing less.

Most importantly I thank my wife Kacy. She followed me far from home and never doubted me. I thank God for her, and for all His blessings.

Abstract

Cone beam computed tomography (CBCT) is a recent development in radiotherapy for use in image guidance. Image guided radiotherapy using CBCT allows visualization of soft tissue targets and critical structures prior to treatment. Dose escalation is made possible by accurately localizing the target volume while reducing normal tissue toxicity. The kilovoltage x-rays of the cone beam imaging system contribute additional dose to the patient. In this study a 2D reference radiochromic film dosimetry method employing GAFCHROMIC™ model XR-QA film is used to measure point skin doses and dose profiles from the Elekta XVI CBCT system integrated onto the Synergy linac. The soft tissue contrast of the daily CBCT images makes adaptive radiotherapy possible in the clinic. In order to track dose to the patient or utilize on-line replanning for adaptive radiotherapy the CBCT images must be used to calculate dose. A Hounsfield unit calibration method for scatter correction is investigated for heterogeneity corrected dose calculation in CBCT images. Three Hounsfield unit to density calibration tables are used for each of four cases including patients and an anthropomorphic phantom, and the calculated dose from each is compared to results from the clinical standard fan beam CT. The dose from the scan acquisition is reported and the effect of scan geometry and total output of the x-ray tube on dose magnitude and distribution is shown. The ability to calculate dose with CBCT is shown to improve with the use of patient specific density tables for scatter correction, and for high beam energies the calculated dose agreement is within 1%.

ABRÉGÉ

La tomographie par faisceaux conique (CBCT) informatisée a été récemment développée en radiothérapie pour l'utilisation de guidage par imagerie. La radiothérapie guidée par imagerie (IGRT) utilisant le CBCT, permet la visualisation des cibles à tissus mous et des structures critiques avant le traitement. En localisant précisément la cible, une « escalade » de dose est rendue possible et la toxicité des tissus sains est réduite. Les rayons-X à basse énergie (kilovoltage) du system d'imagerie du CBCT, contribue à une dose additionnelle pour le patient. Dans cette étude, une méthode dosimétrique utilisant un film 2D radiochromic (Gafchromic film, model XR-QA) a été employé pour mesurer des points de dose à la peau ainsi que des profiles de dose. Cette étude a été réalisée à l'aide d'un system d'Elekta XVI CBCT installé sur un accélérateur linéaire du Synergy. Le contraste des images quotidiennes du CBCT des tissus mous rend possible au niveau clinique l'utilisation de la radiothérapie adaptive. Dans le but de suivre la dose administrée au patient ou utiliser de la replanification en ligne pour la radiothérapie adaptive, les images CBCT doivent être utilisées pour le calcul de dose. Une calibration des unités de Hounsfield par méthode de correction de dispersion est examinée dans le cas de dose calculée dans des milieux hétérogènes pour les images CBCT. Trois unités de Hounsfield par table de calibration de densité sont utilisées pour chaque des quatre cas incluant des patients et un fantôme anthropomorphique. Le calcul de dose pour chaque cas est comparé avec les résultats cliniques standards de tomographie par faisceaux en éventail. La dose acquise avec le scanner est reportée et l'effet géométrique du scanner ainsi que le débit total du tube a rayon-X sur la magnitude et la distribution de la dose sont montrés. La capacité de calculer la dose avec un CBCT est présentée dans le but d'améliorer l'utilisation de densité spécifique du patient pour la correction de dispersion et pour les faisceaux à haute énergie, la validation du calcul de dose est sous les 1%.

Table of Contents

LIST OF TABLES

LIST OF FIGURES

Chapter 1: Introduction

1.1 Image Guided Radiation Therapy

Modern radiation therapy is by nature image-based. Imaging plays a role in every step of the radiotherapy process starting at diagnosis and continuing through simulation, treatment planning, treatment delivery, and post treatment follow-up. Advances in radiotherapy over the last forty years have followed closely with advances in medical imaging. The introduction of computed tomography (CT) into clinical use in the 1970's made it possible for physicians to peer into the human body, visualizing three dimensional soft tissue anatomy in a non-invasive way. The use of planar radiographs prior to the advent of CT had made it difficult to visualize soft tissue targets and limited the planning of treatments to a two dimensional (2D) endeavour. With the three dimensional (3D) imaging available with CT came three dimensional conformal radiotherapy (3DCRT) having the ability to conform dose distributions to internal targets and away from critical structures. 3DCRT is a treatment method in which 3D images of the patient are used to define a target volume, and individual beams are shaped to conform to the shape of the target as seen from the 2D beam's-eye-view. [1] This increased level of conformity, in theory, allows dose escalation to the target while improving the therapeutic ratio. The introduction of 3DCRT has brought clinical gains including increased tumor control for prostate cancer[2] and preservation of saliva after treatment of head and neck cancers[3], leading to an improved quality of life for patients.

Advances in treatment planning software, computer controlled treatment machines, and the introduction of intensity modulated radiotherapy (IMRT) have greatly increased the level of conformity possible in external beam radiation therapy plans.[4-6] Associated with highly conformal therapies is a steep dose gradient outside of the planned target volume (PTV). The rapid fall-off in dose demands accurate delineation of the target during planning and accurate localization of the target during treatment to avoid under-dosing of the malignancy.[7] Sufficient accuracy can be achieved with the proper use of emerging imaging techniques.

Image guided radiation therapy (IGRT) is a term currently used to describe emerging radiation planning, patient setup, and delivery techniques that utilize image based target definition methods, patient immobilization devices, and delivery guiding tools. There are four key areas of IGRT: Biological imaging for target delineation, time resolved imaging to account for intra-fraction motion, on-board imaging to accurately locate the target volume and correct setup errors, and new planning and delivery techniques to incorporate the information gained through new imaging techniques often referred to as adaptive radiotherapy (ART).[1] This thesis focuses on the last two of these areas.

1.1.1 The Need for Accurate Target Localization

Treatment planning is done on the basis of image sets taken at the beginning of the radiotherapy workflow. These can include CT or nuclear magnetic resonance (MRI) anatomical images, as well as co-registered biological images from positron emission tomography (PET) and single photon emission computed tomography (SPECT). The visible extent of the tumor in these images, or as defined in the ICRU report 50 "...the gross palpable or visible/demonstrable extent and localization of malignant growth," is known as the gross tumor volume (GTV).[8] ICRU reports 50 and 62 define the principle volumes for radiotherapy planning.

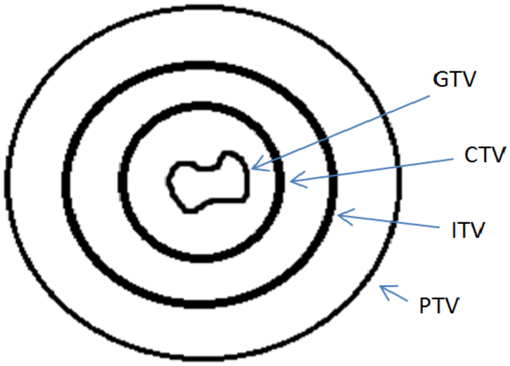

Figure 1.1: Illustration of principle volumes for radiotherapy planning: Gross tumor volume (GTV), clinical target volume (CTV), internal target volume (ITV), and planning target volume (PTV).[8,9]

In order to encompass possible microscopic malignancies surrounding the visible tumor and other possible areas at risk (such as positive lymph nodes) the GTV is expanded to form the clinical target volume (CTV).[10] About this expansion are two subsequent expansions: Internal target volume (ITV) and planning target volume (PTV). These volumes are used to account for mechanical uncertainties, inter-fractional and intra-fractional motion of the target, and setup errors. It is common in clinical practice to drop the ITV and account for all uncertainty with the PTV. The larger the uncertainty in motion or setup, the larger must be the PTV. The larger the PTV, the more healthy tissue is irradiated, limiting the amount of dose that may be given to the target and decreasing the therapeutic ratio.

Intra-fractional motion, the motion of anatomy during a treatment fraction, is attributable to respiratory motion and to a lesser extent differential filling of organs and various other anatomical considerations and in most cases must be accounted for during treatment planning in the form of an increase in the PTV margin. Inter-fractional errors, due to the motion of anatomy between treatment days or between the planning simulation and subsequent treatment days, occur in part due to the use of skin marks to align the patient's anatomy to the treatment room isocenter. Skin marks and internal anatomy are not always well correlated.[11,12] Millender et. al. showed the mean positioning error of obese prostate patients to be 11.4 mm in the left-right direction and 7.2 mm in the superoinferior direction, when aligned by skin marks.[13] Not only do these uncertainties necessitate a larger margin in the PTV but they increase the probability of a geometrical miss, thereby under-dosing the target and increasing the occurrence of healthy tissue toxicity. These inter-fractional errors can be corrected at the time of treatment through the use of IGRT.

Well established IGRT methods include the use of 2D mega-voltage (MV) radiographs acquired with either film or electronic portal imaging devices (EPID). In this approach orthogonal planar radiographs are acquired and the patient is aligned by registering the pre-treatment image to digitally reconstructed radiographs (DRR) or simulation verification portal images based on bony anatomy visible in the images. Poor soft tissue contrast is a major problem of this approach.[1] Implanted radio-opaque fiducial markers (FM) can be surgically implanted into soft tissues such as the prostate to guide patient alignment for this 2D approach. Kilovoltage orthogonal radiographs can be used as well with improvement in contrast for bony structures, though soft tissue imaging and correction of daily organ motion is still limited.[1]

Figure 1.2: IviewGT™ Mega-voltage portal imager (Photo courtesy of Elekta, Stockholm, Sweden)

Improved soft tissue contrast and volumetric (3D) images can be obtained in-room with approaches including ultrasound and CT on rails. Transabdominal ultrasound has been used for pelvis and upper abdominal IGRT,[14] though ultrasound suffers air and bone artifacts, and high inter-user variability.[15] CT on rails, or in-room CT, is a diagnostic quality CT scanner in the treatment room with its own isocenter registered to that of the linear accelerator (linac). CT on rails provides excellent soft-tissue contrast and volumetric images for proper alignment of the target volume to the linac isocenter, though in practice the isocenters are not coincident[16] and the system relies on the mechanical stability of two independent systems.[1]

A more recent advancement in volumetric IGRT is cone-beam computed tomography. Cone-beam computed tomography (CBCT) based upon flat-panel technology and integrated into a linac for image guidance has become available in recent years for use in the clinic.[1] The clinical application of CBCT entails acquiring a volumetric image of the patient in the treatment position and registering this image to a reference planning CT image via an integrated software system. The registration, whether manual or automatic, allows the software system to calculate the necessary patient shift to align the planned isocenter to the linac isocenter. Mega-voltage CBCT has been reported on by Pouliot et. al. and supplies sufficient resolution to register images by air cavities and bony structures with millimeter precision.[17,18] Kilo-voltage CBCT supplies superior soft-tissue contrast compared with MV CBCT, and achieves superior patient alignment to 2D methods, with localization improvement of 2mm when translational shifts are used for alignment. Current kV CBCT software is capable of not only translational shift calculation, but of rotational as well, able to detect rotational setup errors as small as 2°.[1] The goal of IGRT is to find the offset of the target relative to its planned position, and the volumetric soft-tissue contrast of kV CBCT provides an elegant solution. Den et. al. found that CTV to PTV margins could be reduced by as much as 50% for head and neck cancer patients undergoing daily IGRT with kV CBCT.[19] This sort of reduction in PTV margins allows escalation of dose, reduction in radiation toxicity, and better local tumor control. These benefits come with the cost of increased capital and operating costs, and an increase in additional radiation dose delivered to the patient by the scan acquisition itself. Though the improvement in patient localization with CBCT is only slightly better than with less expensive 2D IGRT methods, the volumetric soft-tissue CBCT images offer a new avenue for radiotherapy. By detecting changes in anatomy, whether it is weight loss, tumor shrinking, or systematic errors, CBCT can prompt clinicians to change the treatment plan when certain thresholds are met; an emerging process referred to as adaptive radiotherapy.

1.1.2 Cone Beam CT Based Dose Calculation

Patient shifts based upon soft tissue or bony anatomy are not always sufficient to ensure the planned dose distribution is realized in the clinic. In cases where there has been a significant change in patient anatomy due to weight loss or deformation of surrounding organs, no shift can properly ensure the proper dose is delivered. The ideal solution may be an adaptive radiotherapy (ART) approach utilizing active on-line replanning to accommodate the present anatomy.[20,21] One possible technique is to use the daily CBCT image to create the adapted treatment plan. Even in cases where no replanning is needed dose tracking for organs at risk could be improved by finding the “dose-of-the-day” using the daily

IGRT CBCT images. Both of these ART techniques require use of the CBCT data set for dose calculation in the treatment planning system. The dosimetric feasibility of CBCT data sets for calculating dose has been studied and reported on.[22-26] Fan-beam CT has been used as the gold standard in radiation therapy treatment planning, and has been validated for dosimetric accuracy.[23] Cone-beam CT on the other hand is a newer technology and work is still being done to understand what ability it has for treatment planning in the clinic.

1.2 Thesis Objective

There are two objectives to this project. The first is to measure the dose distribution and point skin dose to a patient from the acquisition of a daily cone-beam CT scan on the Elekta XVI system (XVI v. 4.2, Elekta, Crawley, UK). The second is to evaluate the accuracy of dose calculations based on XVI cone-beam CT data sets compared to planning CT based calculations.

References for Chapter 1

1. Xing, L.; Thorndyke, T.; Eduard, S.; Yang, Y.; Li, T.F.; Kim, G.Y.; Luxton, G.; Koong, A. Overview of Image-Guided Radiation Therapy. *Med. Dosim.* **31:** 91-112; 2006
2. Pollack, A.; Zagars, G.K.; Starkschall, G.; et. al. Prostate Cancer Radiation Dose Response: Results of the MD Anderson phase III Randomized Trial. *Int. J. Radiat. Oncol. Biol. Phys.* 2002; **53** 1097-1105
3. Eisbruch, A.; Dawson, L.A.; Kim, H.M.; et. al. Conformal and Intensity Modulated Irradiation of Head and Neck Cancer: The Potential for Improved Target Irradiation, Salivary Gland Function, and Quality of Life. *Acta Otorhinolaryngol Belg* 1999; **53**: 270-275
4. IMRT Collaborative Working Group: Intensity-modulated radiotherapy: Current status and issues of interest. *Int. J. Radiat. Oncol. Biol. Phys*. **51**:880 –914; 2001.
5. AAPM IMRT Sub-Committee: Guidance document on delivery,treatment planning, and clinical implementation of IMRT: Report of the IMRT Subcommittee of the AAPM Radiation Therapy Committee. *Med. Phys*. **30**:2089 –115; 2003.

6. Galvin, J.M.; Ezzell, G.; Eisbrauch, A.; *et al.* Implementing IMRT in clinical practice: A joint document of the American Society for Therapeutic Radiology and Oncology and the American Association of Physicists in Medicine. *Int. J. Radiat. Oncol. Biol. Phys.* **58:**1616–34; 2004.
7. Mackie, T.R.; Kapatoes, J.; Ruchala, K.; et.al. Image Guidance for Precise Conformal Radiotherapy. *Int. J. Radiat. Oncol. Biol. Phys.* **56:** 89-105, 2003
8. ICRU Report 50: Prescribing, Recording and Reporting Photon Beam Therapy. *Med. Phys.* 21: 833-834, 1994
9. Prescribing, Recording and Reporting PhotonBeam Therapy (Supplement to ICRU Report50), ICRU Report 62. By ICRU, pp. ix+521999 (ICRU, Bethesda, MD)
10. E. B. Podgorsak, "Radiation Oncology Physics : A handbook for teachers and students", (IAEA, 2005), pp.221
11. Hoisak, J.D.; Sixel, K.E.; Tirona, R.; et. al. Correlation of Lung Tumor Motion with External Surrogate Indicators of Respiration. *Int. J. Radiat. Oncol. Biol. Phys.* **60**: 1298-1306, 2004

12. Schallenkamp, J.M.; Herman, M.G.; Kruse, J.J.; et. al. Prostate Position Relative to Pelvis Bony Anatomy Based on Intraprostatic Gold Markers and Electronic Portal Imaging. *Int. J. Radiat. Oncol. Biol. Phys.* **63**: 800-811, 2005

13. Millender, L.E.; Aubin, M.; Pouliot, J.; et. al. Daily Electronic Portal Imaging for Morbidly Obese Men undergoing Radiotherapy for Localized Prostate Cancer. *Int. J. Radiat. Oncol. Biol. Phys.* **59**: 6-10, 2004

14. Dawson, L.A.; Jaffray, D.A.; Advances in Image Guided Radiation Therapy. *Journal of Clinical Oncology* **25**: 938-946, 2007

15. Dawson, L.A.; Jaffray, D.A.; Image-Guided Radiotherapy; Rationale, Benefits, and Limitations. *Lancet Oncol.* **7**: 848-858, 2006

16. Uemetsu, M.; Fukui, T.; Shioda, A.; et. al. A Dual Computed Tomography Linear Accelerator Unit for Stereotactic Radiation Therapy: A New Approach without Cranially Fixated Stereotactic Frames. *Int. J. Radiat. Oncol. Biol. Phys.* **35**: 587-592, 1996

17. Jaffray, D.A.; Siewerdsen, J.H.; Wong, J.W.; et. al. Flat-panel Cone-beam Computed tomography for Image Guided Radiation Therapy. *Int. J. Radiat. Oncol. Biol. Phys.* **53:** 1337-1349, 2002

18. Pouliot, J.; Bani-Hashemi, A.; Chen, J.; et. al. Low-Dose Mega-voltage Cone-beam CT for Radiation Therapy. *Int. J. Radiat. Oncol. Biol. Phys.* **61:** 552-560, 2005
19. Den, R.B.; Doemer, A.; Machtay, M.; et. al. Daily Image Guidance with Cone-beam Computed Tomography for Head-and-Neck cancer Intensity-Modulated Radiotherapy: A Prospective Study. *Int. J. Radiat. Oncol. Biol. Phys.* In Press, 2009
20. Mohan, R.; Zhang, X.; Wang, H.; et. al. Use of Deformed Intensity Distributions for On-line Modification of Image-guided IMRT to Account for Interfractional Anatomic Changes. *Int. J. Radiat. Oncol. Biol. Phys.* **61**: 1258-1266, 2005
21. Wu, C.; Jeraj, R.; Olivera, G.; et. al. Re-optimization in Adaptive Radiotherapy. *Phys. Med. Biol.* **47**: 3181-3195, 2002
22. Yang, Y.; Schreibmann, E.; Li, T.; Wang, C.; Xing, L.; Evaluation of On-board kV Cone Beam CT (CBCT)-based Dose Calculation. *Phys. Med. Biol.* **52**: 685-705, 2007
23. Yoo, S.; Yin, F.F.; Dosimetric Feasibiltiy of Cone-beam CT-based Treatement planning compared to ct-based treatment planning. *Int J Radiat Oncol Biol Phys* **66**: 1553-1561, 2006

24. Hatton, J.; McCurdy, B.; Greer, P.B.; Cone beam computerized tomography: the effect of calibration of the Hounsfield unit number to electron density on dose calculation accuracy for adaptive radiotherapy. *Phys. Med. Biol.* **54**: N329-N346, 2009
25. Létourneau, D.; Wong, R.; Mosely, D.; et. al. Online planning and delivery technique for radiotherapy of spinal metastases using cone-beam CT: image quality and system performance. *Int. J. Radiat. Oncol. Biol. Phys.* **67**: 1229-1237, 2007
26. Richter, A.; Hu, Q.; Steglich, D.; et. al. Investigation of the usability of conebeam CT data sets for dose calculation. *Radiation Oncology* **3**: 2008

Chapter 2: Interaction of Radiation with Matter

When radiation passes through a material, interaction between the radiation and matter can occur. Radiation interacts with the atoms of a material through processes which produce excitation and ionization. Ionization refers to the removal of an orbital electron, leaving the interacting atom in a positively charged state. Ionizing radiation is considered to be any radiation of sufficient energy to liberate orbital electrons through interaction. Of all ionizing radiation there are two types: Directly ionizing, and indirectly ionizing.

Directly ionizing radiation includes charged particles such as electrons, protons, and α-particles, which ionize through large numbers of interactions, incrementally losing energy along their path. Some interactions along the track-length can eject orbital electrons, known as δ-rays, with enough energy to cause further ionizations.

Indirectly ionizing radiation includes neutral particles such as neutrons and photons. These particles make few interactions before expending their energy, and liberate directly ionizing particles.[1]

2.1 Interaction of Photons with Matter

When a beam of photons is incident upon a scattering medium, a portion of the photons will interact, while the rest pass through unaffected. The number of interactions (n) in the medium will depend upon the initial number of photons (N_o), the thickness of the scattering medium (Δ x), and a constant of proportionality (μ), referred to as the linear attenuation coefficient[2], where

$$n = \mu \, N_o \, \Delta x \tag{2.1}$$

The linear attenuation coefficient is a function of the nature of the attenuating material and the energy of the radiation, and has units of inverse distance. When a photon interacts with the medium it is removed from the primary beam by scattering or absorption in the material. The number of interactions is equal to the negative of the change in the number of photons (ΔN) :

$$n = -\Delta N \tag{2.2}$$

Substituting equation 2.2 into 2.1 yields,

$$\Delta N = -\mu \cdot N \cdot \Delta x \tag{2.3}$$

This equation holds true only if the number of photons traversing the medium is constant. The finite size of Δx means that the number of photons will decrease as the beam traverses the medium, so that equation 2.3 is only an approximation.

If Δx is allowed to approach zero then expression 2.3 becomes a differential equation which can be solved by calculus to yield the exponential attenuation equation:

$$N = N_{\circ} \cdot e^{-\mu x} \tag{2.4}$$

Whereas equation 2.3 only applies when the layer removes a small number of photons meaning either μ or Δx is very small, this equation may be used to calculate the number of photons which will pass through a given material of any thickness x. This equation is equally valid for finding the intensity (I) of a photon beam after passing through a scattering medium:

$$I = I_{\circ} \cdot e^{-\mu x} \tag{2.5}$$

The half-value layer (HVL) for a monoenergetic beam, defined as the thickness of a given material required to attenuate a photon beam to one half of its original intensity, is of interest in characterizing diagnostic range photon beams and can be calculated from equation 2.5 by solving for the case when $I = \frac{1}{2} I_{\circ}$, and $x = HVL$:

$$HVL = \frac{0.693}{\mu} \tag{2.6}$$

The HVL of a given beam may be found experimentally by graphing the measured remaining intensity as a function of absorber thickness, as illustrated in figure 2.1.

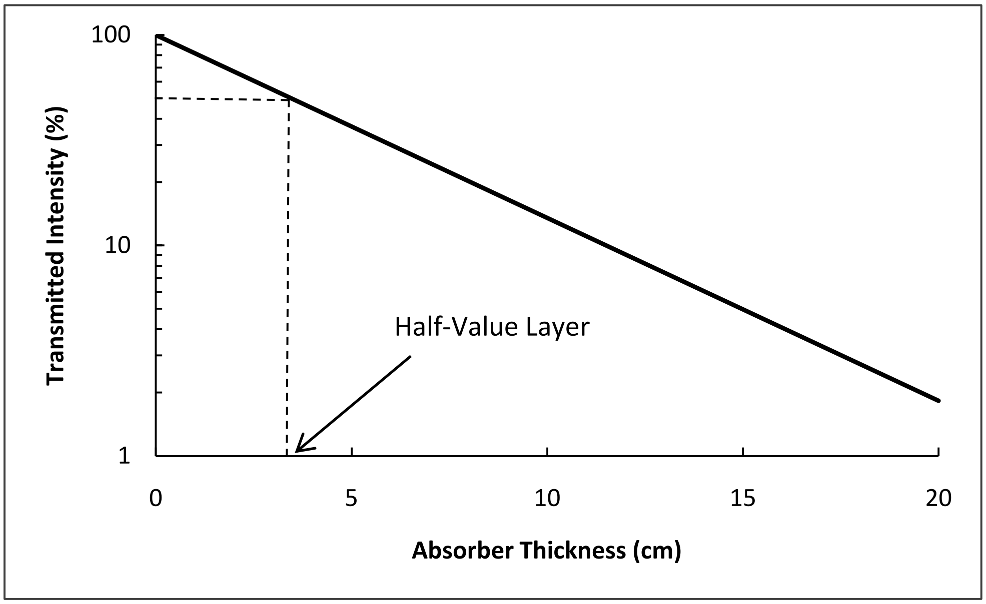

Figure 2.1: Percent transmission for a monoenergetic beam as a function of absorber thickness ($\mu = 0.2\ cm^{-1}$).

Exponential attenuation of this nature applies only to monoenergetic beams.[1] Practical x-ray beams produced in medicine consist of a spectrum of photon energies. The absorber will attenuate the photons differently depending upon where they lie in the spectrum, and in the diagnostic range of 10-200 kV the absorber will preferentially attenuate the lower energy photons through photoelectric absorption. This effectively changes the attenuation coefficient as the beam passes through the absorbing material so that $HVL_1 \neq HVL_2$. In general the first half-value layer is smaller than subsequent half-value layers.[1] The increase in half-value layer makes the resulting beam more penetrating; a phenomenon known as “beam hardening”.

2.1.1 Attenuation, Energy Transfer, and Energy Absorption Coefficients

The linear attenuation coefficient discussed previously has units of cm^{-1} and depends upon the energy of the photon beam and the characteristics of the absorbing material. The attenuation in a given material depends upon the number of electrons available for interaction and therefore upon the density of the material. By dividing out the physical density (ρ) the resulting coefficient $(\frac{\mu}{\rho})$ is independent from the density of the material. This is known as the mass attenuation coefficient and has units of cm^2/g. The mass attenuation coefficient is more fundamentally useful as it is a factor of the atomic composition of the material and not the physical density.

In photon interactions some or all of the photon energy is given to charged particles as kinetic energy. The fraction of the photon initial energy converted to charged particle kinetic energy per unit of thickness of absorbing material is the energy transfer coefficient (μ_{tr}).[1] Of this energy imparted to charged particles some will be deposited locally through collisional interactions (secondary ionizations and excitations) while some will be radiated away as bremsstrahlung. The fraction of the initial photon energy which will be converted to charged particle kinetic energy and deposited locally per unit of thickness is the energy absorption coefficient (μ_{en}). A useful quantity is the mass energy absorption coefficient ($\frac{\mu_{en}}{\rho}$). This quantity can be used to calculate the energy absorbed in tissues for radiotherapy purposes.

Photon beams may be attenuated by four types of interactions: Coherent scattering, incoherent scattering, photoelectric effect, and pair production. The mass attenuation coefficient described previously is the sum of the individual attenuation coefficients for these four processes[3]:

$$\frac{\mu}{\rho} = \frac{\sigma_{coh}}{\rho} + \frac{\sigma_c}{\rho} + \frac{\tau}{\rho} + \frac{\kappa}{\rho} \tag{2.7}$$

Here σ_{coh} , σ_c , τ , and κ are the attenuation coefficients for coherent scattering, incoherent or Compton scattering, photoelectric effect, and pair production (including triplet production) respectively. Figure 2.2 gives the mass attenuation coefficients for lead as a function of energy.

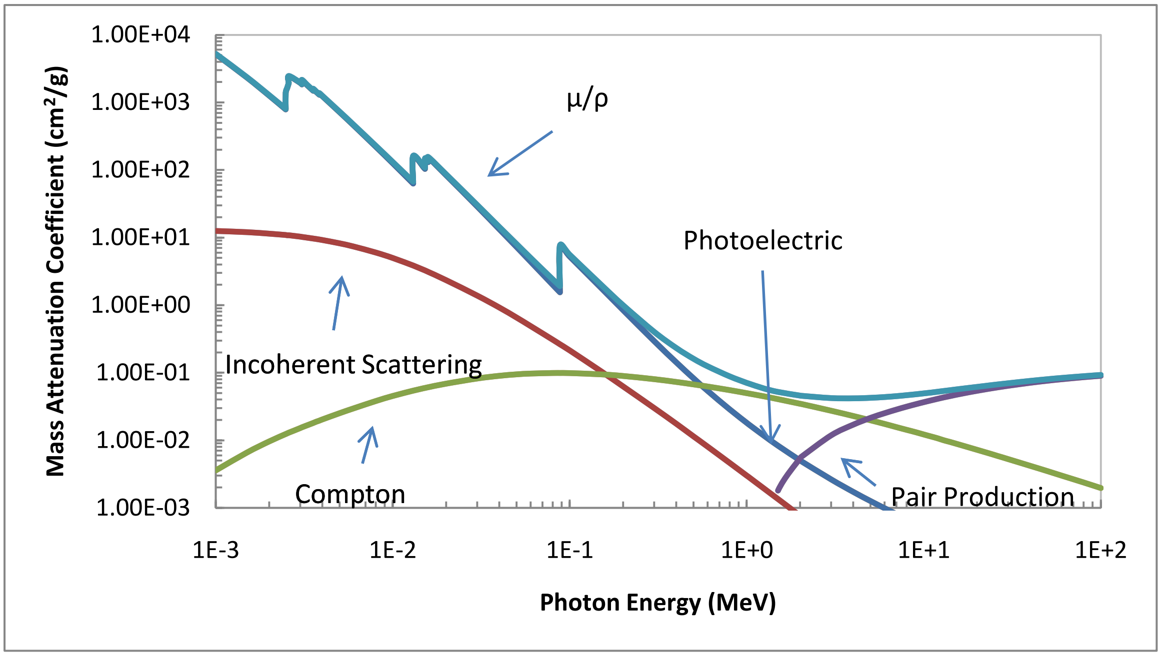

Figure 2.2: Mass attenuation coefficients as a function of energy for lead.[4]

Of these interactions, only Compton scattering, photoelectric effect, and pair production transfer energy, so for radiobiological purposes they are the key interactions of concern. The probability of each interaction is dependent upon atomic number of the absorbing medium and photon energy. The dominant regions for each interaction are illustrated in figure 2.3.

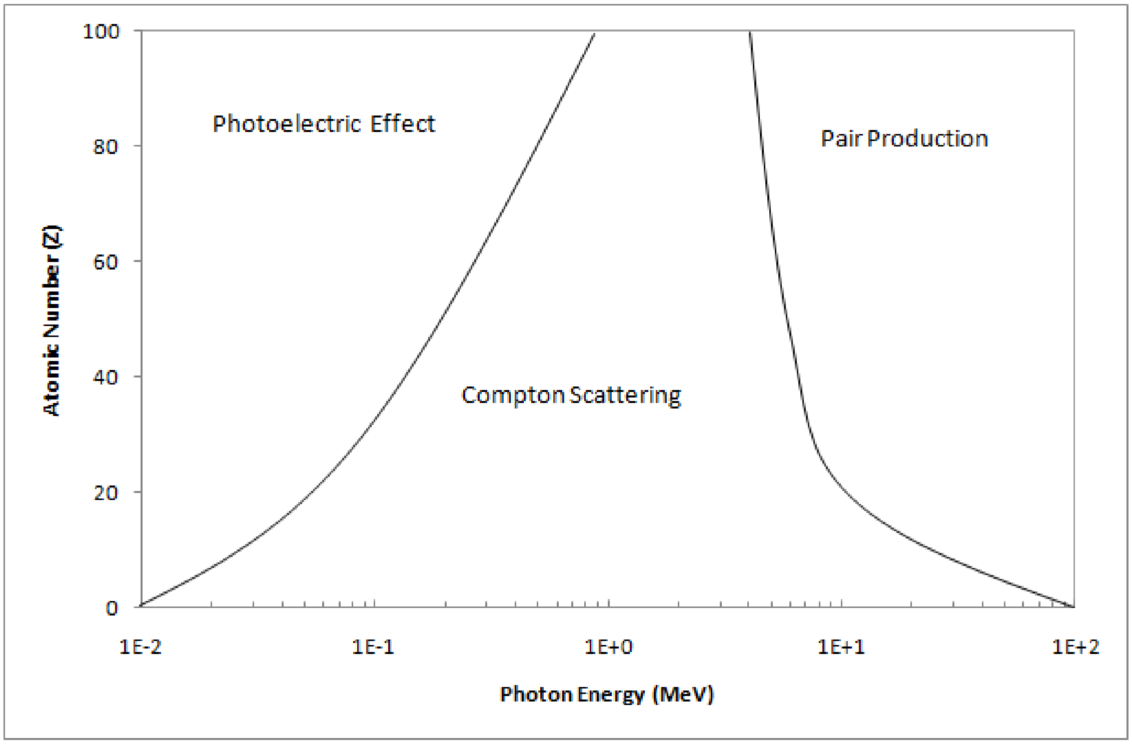

Figure 2.3: Regions of dominance for photon interactions.[3]

2.1.2 Photoelectric Effect

The photoelectric effect is an interaction between a photon and a tightly bound orbital electron. In the interaction, the orbital electron absorbs the photon and all of the energy of the photon ($h\nu$) and is ejected from the atom. The ejected orbital electron, now known as a photo-electron, is left with kinetic energy of $E_K = h\nu - E_B$, where E_B is the binding energy of the orbital electron.[3] The ejection of the electron leaves a vacancy in the shell and the atom in an excited state.[1] The atom can return to the ground state by emission of characteristic radiation or by emission of monoenergetic Auger electrons. The mass attenuation coefficient for the photoelectric effect for several materials is plotted in figure 2.4.

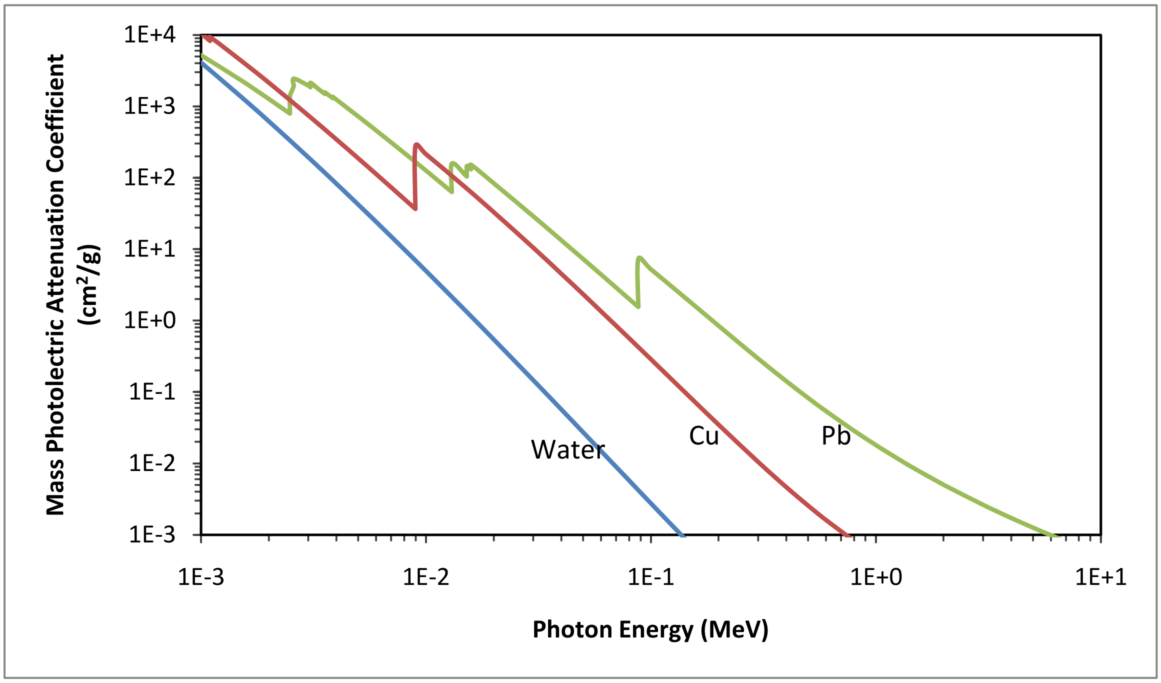

Figure 2.4: Mass attenuation coefficient for photoelectric effect for water, copper, and lead.[4]

The photoelectric effect is dependent upon photon energy and is most likely to occur when the binding energy of the orbital electron is close in magnitude to that of the photon, as can be seen by the sharp peak in cross section present at the K-edges of copper and lead in Figure 2.2. Below the K-edge the photons lack sufficient energy to ionize the K shell electrons and are therefore limited to the L and lower shells. At 88 keV, the binding energy of the K shell electrons for lead, resonance occurs and the probability for photoelectric absorption sharply increases.

When away from absorption edges the graphs in figure 2.2 are nearly straight lines with a slope of about -3, which leads to the relationship between $\frac{\tau}{\rho}$ and photon energy[1]:

$$\frac{\tau}{\rho} \propto \frac{1}{hv^3} \tag{2.8}$$

Data for different materials indicates that the photoelectric effect depends upon atomic number as approximately Z^3. Together with equation 2.8 the dependence of mass photoelectric attenuation upon energy and atomic number is:

$$\frac{\tau}{\rho} \propto \frac{Z^3}{h\nu^3} \tag{2.9}$$

2.1.3 Compton Scattering

The Compton effect, or Compton scattering, is an interaction between a photon and a loosely bound or “free” electron. Here free indicates that the binding energy of the orbital electron is much lower than the energy of the incoming photon. In the process of Compton scattering the incoming photon interacts with the electric field of the free electron scattering the electron at an angle θ, and a photon of reduced energy at an angle ϕ. The energy transferred from the incoming photon to the free electron is a function of the mass of the electron

(0.511 MeV/c^2), the energy of the incoming photon ($h\nu$), and the scattering angle of the outgoing photon ($h\nu'$), and is governed by the following equation[1]:

$$E = h\nu \frac{\alpha(1-\cos\phi)}{1+\alpha(1-\cos\phi)} \tag{2.5}$$

Where $\alpha = \frac{h\nu}{m_\circ c^2}$, and $m_\circ c^2$ is the rest mass energy of the electron (0.511 MeV).

The maximum energy transferred to an electron in a Compton event arises from a photon scattered at an angle of 180° and is the energy of the incoming photon minus half the rest mass energy of an electron: $E = h\nu - 0.255\ MeV$.

The mass attenuation coefficient for Compton scattering for several materials is plotted in figure 2.5.

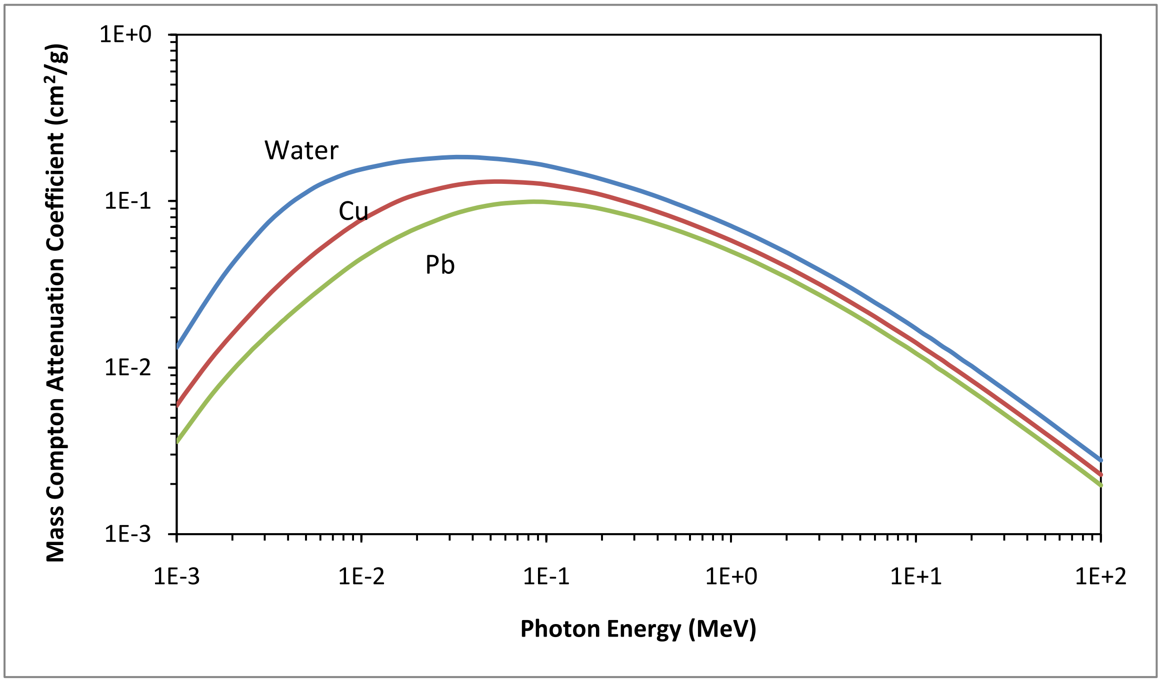

Figure 2.5: Mass Compton attenuation coefficient for water, copper, and lead.[4]

The probability for Compton scattering increases as the photon energy relative to electron binding energy increases, and then begins to decrease. Because Compton scattering involves a photon and a free electron the probability of interaction is nearly independent of Z with the exception of hydrogen. The Z/A ratio for hydrogen is 1, whereas for all other materials the ratio is approximately ½.

2.1.4 Pair Production

In pair production the energy of a photon is completely converted into matter following Einstein's famous equation $E = mc^2$. The process produces an antiparticle pair: One electron and one positron[1]. Due to momentum conservation laws this interaction must take place near a massive particle, usually the nucleus of an atom although at higher energies it is possible for this interaction to occur in the electric field of an orbital electron in a process known as triplet production. Because the interaction in pair production is within the electromagnetic field of the nucleus the probability of this interaction increases with increasing atomic number materials. Because the rest mass energy of each particle is 0.511 MeV the photon must be of at least 1.022 MeV for pair production to occur. Anything above this threshold energy will be shared between the resulting particles as kinetic energy, the most likely distribution of which is for each particle to take half of the total kinetic energy.

The created electron and positron will expend their kinetic energy through excitation, ionization, and bremsstrahlung (see section 2.2). At the end of its track length the now low energy positron will interact with an electron in an annihilation process resulting in two photons with energy of 0.511 MeV each. Because momentum is conserved, the photons will be emitted at an angle of almost (as the positron and electron are never completely at rest) 180° to one another. These photons can subsequently interact with the material inducing further ionizations and excitations.

2.2 Interaction of Electrons with Matter

The energy transferred in a single interaction between high energy electrons and the atoms of an absorbing medium is generally small resulting in a large number of interactions in which the electron loses energy gradually.[3] There is a finite distance over which an electron can excite and ionize after which all the energy is spent and no more particles are produced. This is in contrast with photon interactions in which the attenuation is exponential in nature and there is no finite thickness which will completely absorb the beam.[2]

The energy transferred in interactions between electrons and the atoms of an absorber is described by the stopping power (S), which is the rate of energy loss per unit path length by a charged particle in a medium. It is often given as mass stopping power $(\frac{S}{\rho})$ with units of $MeV \cdot {cm^2}/{g}$. The stopping power is the sum of the energy transferred by radiative and collision interactions[3]:

$$S_{total} = S_{rad} + S_{col} \tag{2.6}$$

2.2.1 Radiative Interactions

Coulombic interaction between electrons and the electromagnetic field of atomic nuclei results in rapid acceleration of the electron and the emission of bremsstrahlung radiation. The energy lost in these radiative interactions per unit length is the radiative stopping power (S_{rad})[3]. The radiative stopping power is a function of electron kinetic energy and atomic number. Above 2 MeV the radiative stopping power is approximately proportional to the atomic number (Z) and increases nearly linearly with energy, as illustrated in figure 2.6.

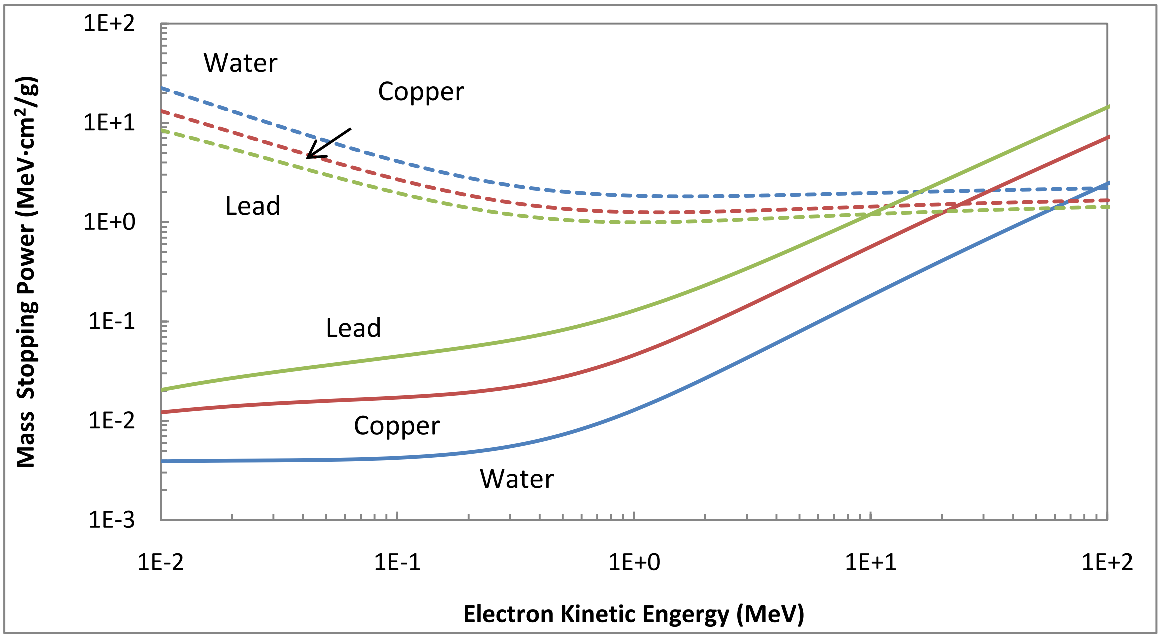

Figure 2.6: Mass stopping powers as a function of electron kinetic energy. Radiative stopping powers are given in solid lines, collision in dashed lines.[4]

2.2.2 Collision Interactions

Coulombic interactions between an incident electron and an orbital electron are considered collision interactions and result in ionization and excitation. The minimum amount of energy that can be transferred in a collision interaction is the excitation potential of the orbital electron, and because the electrons are indistinguishable the maximum energy transfer in a single interaction is half the impinging electron's kinetic energy. The collision stopping power is an important dosimetric quantity.

The linear energy transfer (LET), where the energy loss is restricted to that which will be deposited locally allows calculation of dose and is given by equation 2.7[1]:

$$\left(\frac{L}{\rho}\right)_{col,\Delta} = \left(\frac{dE}{\rho dl}\right)_{col,\Delta} \tag{2.7}$$

Here, Δ represents the restricted energy, the value of which limits the energy of secondary electrons such that they deposit energy within the volume of interest. The distance traveled by a charged particle in a medium is dependent upon the energy of the particle and the nature of the material and in general is referred to as the range.

2.2.3 Charged Particle Range

When traversing an absorbing material charged particles lose energy due to ionization, excitation, and bremsstrahlung. They also undergo many elastic scattering deflections. Electrons and positrons scatter at much larger angles than heavier charged particles such as protons, which traverse matter in a more rectilinear fashion. There are several definitions of range in use and in general range is considered to be the thickness of an absorbing medium that the charged particle can just penetrate. The actual path length is a separate concept from the range and can be calculated as suggested by Berger and Seltzer with the continuous slowing down approximation (CSDA)[3]:

$$R_{CSDA} = \int_{0}^{E_{K_i}} \frac{dE}{S_{tot}(E)} \tag{2.8}$$

Here, E_{K_i} is the initial kinetic energy of the charged particle, $S_{tot}(E)$ is the total stopping power of the charged particle as a function of kinetic energy, and R_{CSDA} is the mean path length of the charged particle. For heavy charged particles whose trajectory is approximately rectilinear the R_{CSDA} is approximately equal to the range. For electrons and positrons the R_{CSDA} is up to twice as long as the range of the charged particle.

2.3 Exposure, Kerma, and Absorbed Dose

In passing through air a beam of photons produces high energy charged particles through Compton scattering, photoelectric effect, and pair production. The quantity *exposure* is a measure of the charge produced in air per unit of mass when all charged particles are completely stopped in air and is given by:

$$X = \frac{dQ}{dm} \tag{2.9}$$

The SI unit of exposure is coulomb per kilogram (C/kg) and its special unit is the Roentgen (R), where $1R = 2.58 \times 10^{-4} C/kg$.

Kerma (kinetic energy released in matter) is the total initial kinetic energy of all charged particles liberated by ionizing photons per unit of mass. Some of this energy will be expended in radiative interactions and some in collision interactions, the ratio of which is dependent upon photon energy and the attenuating material characteristics, and the total kerma can be divided into two parts:

$$K_{tot} = K_{coll} + K_{rad} \tag{2.10}$$

The kerma at a point can be found from the mean mass energy transfer coefficient $\left(\frac{\overline{\mu_{tr}}}{\rho}\right)$ and the photon fluence:

$$K = \Psi\left(\overline{\frac{\mu_{tr}}{\rho}}\right) \tag{2.11}$$

The collision component of kerma is given by:

$$K_{coll} = \Psi\left(\overline{\frac{\mu_{en}}{\rho}}\right) \tag{2.11}$$

The collision kerma in air can thus be found from measured exposure:

$$K_{coll,air} = X \cdot 33.97(C/kg) \tag{2.12}$$

A useful unit in radiotherapy is absorbed dose. It is a measure of the energy absorbed in a given volume per unit of mass with units of joules per kilogram (J/kg), and its special unit is the Gray: 1 Gy = 1 J/kg. Dose can be related to kerma and exposure, described above, which are readily measurable, by considering the properties of the dosimetric system in use and applying appropriate theory. Radiographic films may be used to measure dose by calibrating them in a known beam in terms of dose, kerma, or exposure.

References for Chapter 2:

1. F. M. Khan, "The Physics of Radiation therapy", (Lippincott Williams & Wilkins, 2003), pp. 54, 60-61, 266
2. H.E. Johns, J.R. Cunningham, “The Physics of Radiology” (Thomas Books, 1983), pp. 133-137, 197
3. E.B. Podgorsak, “Radiation Physics for Medical Physicists”, (Springer, 2006), pp. 141, 159-160,219-222, 246
4. National Institute of Standards and Technology, http://physics.nist.gov/PhysRefData/Xcom/html/xcom1.html

Chapter 3: Methods and Materials

3.1 Cone Beam Computed Tomography

Radiography, fluoroscopy, and volumetric imaging of a patient in the treatment position are possible through the implementation of a kV x-ray source and flat-panel detector system integrated with the treatment accelerator. Flat panel-detector based cone beam computed tomography allows imaging of soft tissue targets in the treatment position prior to the treatment fraction for a more precise delivery of planned dose distributions. The system investigated here is the X-ray Volumetric Imager (XVI, v. 4.2, Elekta, Crawley, UK) integrated on the Elekta Synergy linac.

3.1.1 Production of Kilovoltage X-rays

X-rays are produced through the process of bremsstrahlung, and to a lesser extent characteristic radiation, by impinging high energy electrons upon a rotating anode in a vacuum x-ray tube. The XVI system x-ray tube (DU 694, Dunlee, Aurora, IL) is capable of sustaining tube voltages up to 150 kV though clinical protocols typically range from 100-120 kV. The peak voltage or kVp is the highest possible photon energy above which the intensity of the produced photon spectrum drops to zero, which for this tube is 150 keV. The spectrum of photons emitted from the anode is influenced by the target material (RTM/Graphite), inherent and additional filtration, and tube voltage. The photons produced in the target are attenuated as they pass through the thickness of the target material. The low energy photons are attenuated at a high rate due to photoelectric absorption[1] and the resulting spectrum displays a sharp reduction in the number of low energy photons due to this inherent filtration, which for this target is equivalent to 1.0 mm Al at 75 kV. Additional physical filters are placed in the beam path as it exits the tube housing. In addition to the 1 mm Al inherent filtration there is an aluminum cone filter, four 0.5 mm aluminum discs, and a copper filter disc fitted to the x-ray tube at the output window with aluminum equivalence values of 0.6 mm, 2.0 mm, and 0.1 mm respectively. These filters harden the beam, reducing dose to the patient and decreasing scatter, and by pre-hardening the beam reduce beam hardening artifacts in the reconstructed image. An optional compensator placed in the beams path hardens the beam further.

3.1.2 Detection of Kilovoltage X-Rays

Volumetric images in CBCT are reconstructed from a series of 2D projection radiographs. The radiographs are collected by measuring x-ray fluence at the detector panel as the gantry rotates about the patient. The amorphous silicon large-area flat-panel detector (FPD) has an active area of 41 x 41 cm^2 and detects x-ray energy in an indirect conversion process[2]. The FPD consists of five layers, illustrated in figure 3.1.

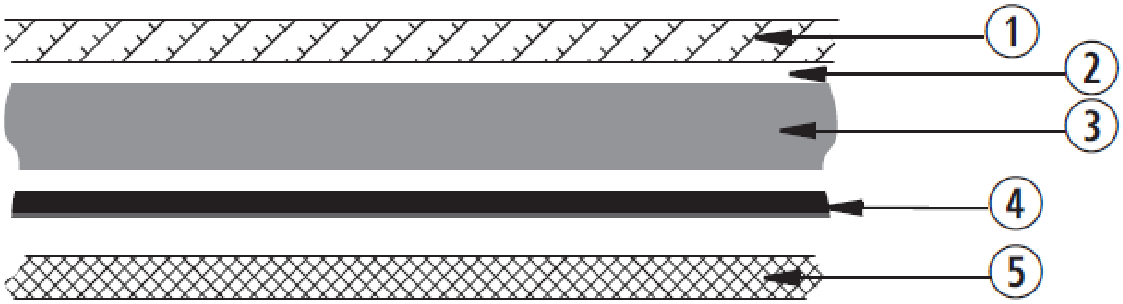

Figure 3.1: Construction of a-Si detector panel. 1-Aluminum, 2-air gap, 3-CsI scintillator, 4-attenuator, 5-photodiodes.[3] (Image courtesy of Elekta, Stockholm, Sweden)

As the photons pass through the FPD the first layer of aluminum removes low energy photons from the beam which then interacts with the CsI scintillator crystals producing 310 nm wavelength bursts of visible light. This light is channelled to an amorphous silicon detector panel where the light energy is converted into electric charges which are collected by capacitors in the thin film transistor (TFT) layer of the photodiode and read out at a nominal frame rate of

5.5 Hz. The amount of charge collected is proportional to the x-ray fluence. The capacitor and TFT form individual pixels of which the array consists of 1024x1024 for a total of 1,048,576 pixels in the array. The dimensions of the array allow measurement of photon fluence spanning 26 cm by 26 cm at the isocenter.[3]

3.1.3 Geometry

The XVI hardware consists of a kilovoltage x-ray source and flat panel detector (FPD) mounted onto the drum of the accelerator gantry. The central axis of the kV beam is oriented orthogonal to the MV treatment beam of the linac. The FPD is mounted opposite of the x-ray source, as illustrated in figure 3.2.

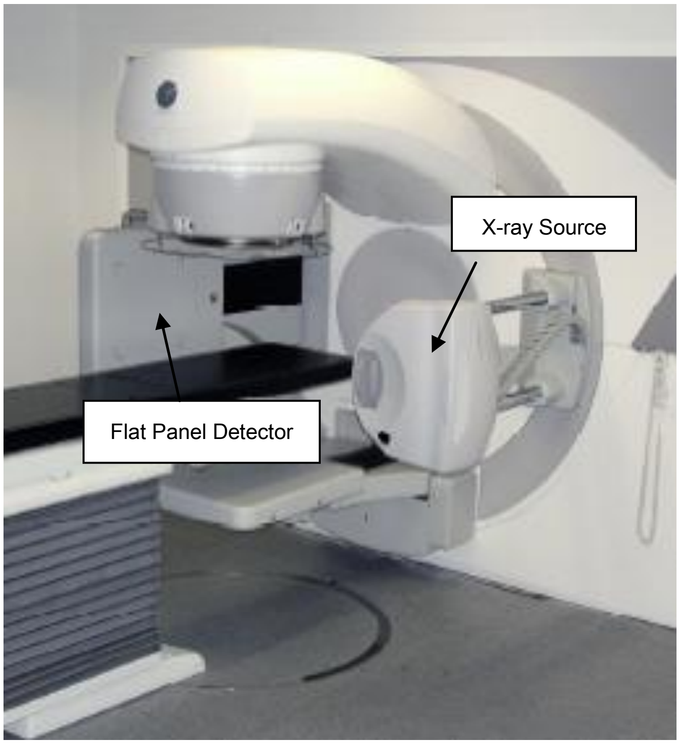

Figure 3.2: kV X-ray source and kV flat panel detector mounted isocentrically to the accelerator gantry (XVI, Elekta, Crawley, UK).[2] (Photo courtesy of Elekta, Stockholm, Sweden)

The x-ray beam is collimated after it leaves the source by collimation cassettes. The cassettes have an aperture cut out from a lead sheet with a thickness of 3.2 mm, controlling the orientation and dimensions of the transmitted photon beam at the isocenter. Figure 3.3 is an example of the collimator cassettes available for this system.

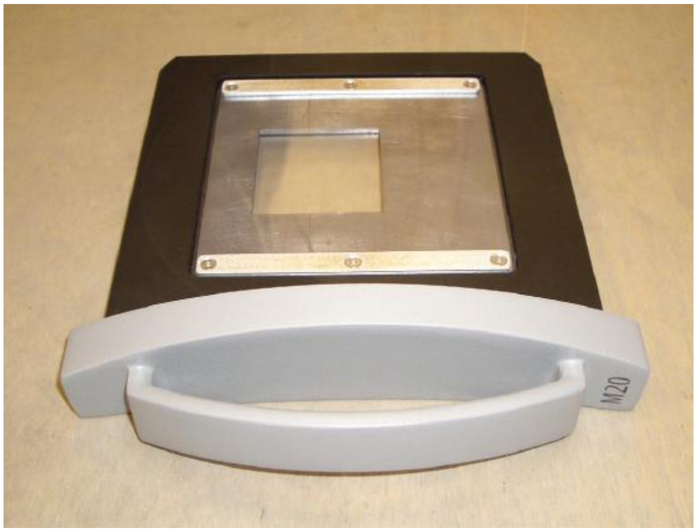

Figure 3.3: Collimation cassette for medium field of view, axial label 20.[4] (Photo courtesy of Elekta, Stockholm, Sweden)

The collimation controls the field-of-view (FOV) in the axial plane and the longitudinal length irradiated at the isocenter. There are three FOV available: Large; 50 cm, medium; 41 cm, and small; 27 cm. Figure 3.4 shows a schematic diagram of the geometry of the small FOV.

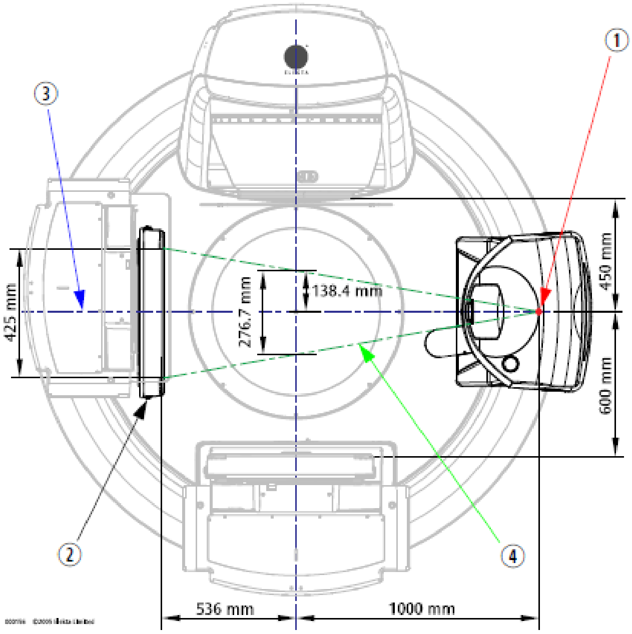

Figure 3.4: Geometry of the small FOV. Central axis of the x-ray tube is in line with that of the aSi FPD.[2] [1] kV x-ray focal spot. [2] FPD. [3] kV beam reference axis. [4] Projected x-ray field. (Photo courtesy of Elekta, Stockholm, Sweden)

The FOV can be increased by shifting the FPD laterally and collimating the beam with the appropriate collimator cassette so that the edges of the beam are still incident upon the edges of the active area. This is known as half-fan (HF) geometry. Scan protocols using the HF geometry of the medium and large FOV require 360° gantry rotation to complete the acquisition. When the FPD is centered for the small FOV the geometry is referred to as full-fan (FF) and requires a gantry rotation of 200°.

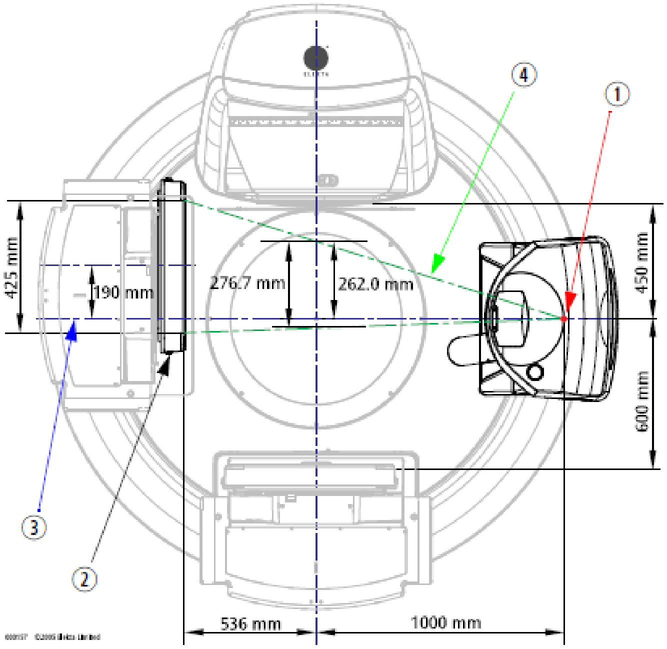

Figure 3.5: Geometry of the large FOV. The FPD is shifted laterally by 19 cm.[2] [1] kV x-ray focal spot. [2] FPD. [3] kV beam reference axis. [4] Projected x-ray field. (Photo courtesy of Elekta, Stockholm, Sweden)

The axial length irradiated along the gantry-target axis can be controlled as well using the collimating cassettes. The selection of axial length value will determine the superoinferior distance visible in the reconstructed image. Table 3.1 lists the axial labels and their corresponding irradiated lengths at the isocenter.

Table 3.1: Axial value labels and the corresponding axial length irradiated at isocenter.[2]

Label	Axial Length Irradiated at Isocenter (cm)
2	3.52 (Medium FOV) 3.65 (Large FOV)
10	13.54 (Medium FOV) 14.32 (Large FOV)
20	27.7
15	17.85 (Medium FOV)
15x15	15.0

The large fields used in CBCT, large irradiated areas, and large detector sensitive area create a condition of increased scatter when compared to the fan-beam geometry of simulation CT scanners. This scatter, as well as detector dynamic range and patient dose considerations, necessitates the use of compensators for clinical applications.

3.1.4 Compensators

As the photon beam passes through the patient some photons are absorbed while others are scattered. Due to the large field sizes in CBCT and the large area of the FPD the amount of scattered radiation reaching the detector can be quite high. In some CBCT geometries such as in the pelvic region the scatter radiation reaching the detector panel can exceed the primary radiation.[5] The scatter reduces contrast, reduces detector quantum efficiency (DQE) in an additive way, and introduces streaking and cupping artifacts. Several methods for scatter management exist but have limitations. Scatter rejection grids can improve the primary to scatter ratio but reduce primary fluence at the detector. Increasing the patient to detector distance will reduce measured scatter but also requires an increase in exposure to maintain sufficient signal to noise ratio. Additionally, the optimum magnification for image quality in this system is coincidentally the same as is already in use in the XVI system (M=1.6) so that an increase in distance would decrease image quality. Ultimately these methods can reduce the measurement of scattered radiation at the detector plane but will not reduce the scattering of low energy photons within the patient which contribute dose but don't improve image quality. Finally, the geometry of the beam leads to the potential for over-reaching the dynamic range of the FPD which is 70 dB. By setting the exposure at a level where a sufficient signal is obtained through the midline of the patient the signal at the periphery of the field can reach a level too high for the dynamic range of the detector panel. For these reasons a compensator is used in most clinical applications.

The compensator is constructed of aluminum and is contained in a cassette that is inserted in the beam path adjacent to the collimation cassette. A diagram of the bowtie filter is given in figure 3.6.

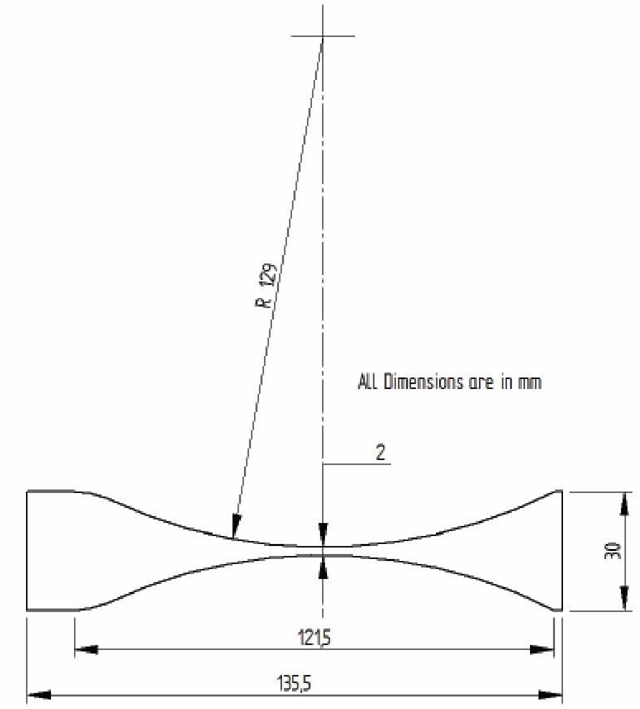

Figure 3.6: Cross section of the aluminum bowtie filter.[2] (Image courtesy of Elekta, Stockholm, Sweden).

The compensator, referred to as a bowtie filter because of its shape, filters out low energy photons, reducing scatter within the patient and thereby reducing dose. It also reduces scatter reaching the detector, improving image quality. Finally its bowtie shape means that photons toward the periphery traverse a greater thickness of aluminum and thereby reduces the signal at the periphery of the field allowing the FPD to operate within its dynamic range. The use of the bowtie filter has been shown to reduce dose and scattered radiation reaching the detector by up to a factor of 2.[5,6]

3.1.5 Clinical Scan Protocols

During commissioning of the X-ray Volumetric Imager a series of clinical scan protocols are created and stored in the controller software for clinical use. These presets are designed for the anatomical region to be imaged and the desired axial length of the reconstruction. The protocols have preset parameters of collimation cassette, filter, kVp, mA/frame, ms/frame, number of frames, and start and stop angle (gantry sweep). A list of preset protocols and their respective parameters is given in table 3.2. These presets were created by an Elekta service engineer for clinical use at Total Cancer Care at Preston Ridge, Alpharetta, GA, and are typical of those presets in use elsewhere.

Table 3.2: Clinical preset scan protocols for XVI v. 4.2. For collimation setting the letter designates the FOV, the number designates the axial value. For filtration F1 is the bowtie filter, F0 is a blank cassette.

NAME	COLLIMATION	FILTER	ENERGY	mA/FRAME	mS/FRAME	# FRAMES	GANTRY ANGLE
Chest	M20	F0	120 kVp	25	40	650	(-)180 to 180
Chest M20 F1	M20	F1	120 kVp	40	40	650	(-)180 to 180
Head and Neck	S20	F0	100 kVp	10	10	361	(-)100 to 100
Head and Neck S10	S10	F0	100 kVp	10	10	361	(-)100 to 100
Pelvis	M20	F0	120 kVp	25	40	650	(-)180 to 180
Pelvis L20 F1	L20	F1	120 kVp	64	40	650	(-)180 to 180
Pelvis M15	M15	F0	120 kVp	25	40	650	(-)180 to 180
Pelvis M15 F1	M15	F1	120 kVp	40	40	650	(-)180 to 180
Pelvis M20 F1	M20	F1	120 kVp	40	40	650	(-)180 to 180
Prostate	M10	F0	120 kVp	40	40	650	(-)180 to 180
Prostate M10 F1	M10	F1	120 kVp	64	40	650	(-)180 to 180
Prostate M15	M15	F0	120 kVp	40	40	650	(-)180 to 180
Prostate M15 F1	M15	F1	120 kVp	64	40	650	(-)180 to 180

3.1.6 Image Reconstruction

As the source and FPD rotate about the patient 2D radiographs are collected and stored for image reconstruction. Up to 650 2D projections are acquired during the scan acquisition depending upon the scan protocol. Before the reconstruction process begins the projections must be pre-processed.

3.1.6.1 Image Pre-Processing

Measurements are acquired during the commissioning of the XVI system to determine pixel variations in offset and gain and identify defective pixels. Flood fields are acquired for each scan protocol with varying parameters of mA, ms, kVp, filter, and FOV. The beam in these measurements is attenuated by a water phantom near enough to the x-ray source that the field dimensions lay within the phantom. The water phantom serves to reduce the fluence at the detector panel to the range expected during scanning of a patient. Defective pixels and those with significant dark field signal are median filtered for use in reconstruction.[7,8]

The significant mass of the x-ray tube and detector panel in combination with their distance from the gantry drum produces a gravity induced flex of these components. Sagging or flexing of the kV source and FPD shifts the kV beam axis relative to the room isocenter during rotation of the gantry. This flex effectively shifts the shadow of the imaged object on the FPD, the magnitude and direction of which is dependent upon the gantry angle at which the projection was binned. If left uncorrected, flex can lead to reduction in the visibility of detail, misregistration, and streak artefacts. To correct for flex a steel ball bearing is placed at the linac isocenter, and its position confirmed by MV portal imaging. The bearing is scanned over 360° and the 2D images binned by gantry angle. The shift necessary to place the centroid of the bearing at the center of the image for each gantry angle is calculated and stored as a flex map. The correction is essentially an in plane translation of the detector panel before back-projection and does not fully correct for the flex of the kV source. Hysteresis effects based on start angle of the gantry and rotation direction (clockwise vs. counter-clockwise) require that flex maps be created for all possible clinical rotation directions and start and stop angles.[7,8,9] These flex maps are then applied to the measured projections before image reconstruction during clinical use.

3.1.6.2 FDK Reconstruction Algorithm

XVI version 4.2 utilizes a convolution-filtered-backprojection algorithm developed by Feldkamp, Davis, and Kress (FDK) in 1984, originally for use in material testing for the Ford motor company. This algorithm operates under the assumption that each 2D fan-shaped surface in the cone must be treated independently with its own angle through the plane of the isocenter[10]. The reconstructed image contains 512x512xN voxels, with the value of N based on the axial length reconstructed. This algorithm has been shown to have adequate computational speed, and its behavior and limitations are well documented.[7,11,12] Puoliot et. al.[13] have shown that CBCT images maintain a sufficiently high level of geometric fidelity, with mean absolute deviations of known positions of less than 1 mm, which is important both for image guidance and TPS dose calculations.

3.1.6.3 Image Registration

Image guidance can now be directed using the reconstructed image of the patient in the treatment position in the reference frame of the treatment room. A reference image from simulation is imported into the XVI software along with contoured regions of interest (ROI). Using the registration tool, the images can be either manually or automatically registered. A screen shot of the registration window is given in figure 3.7.

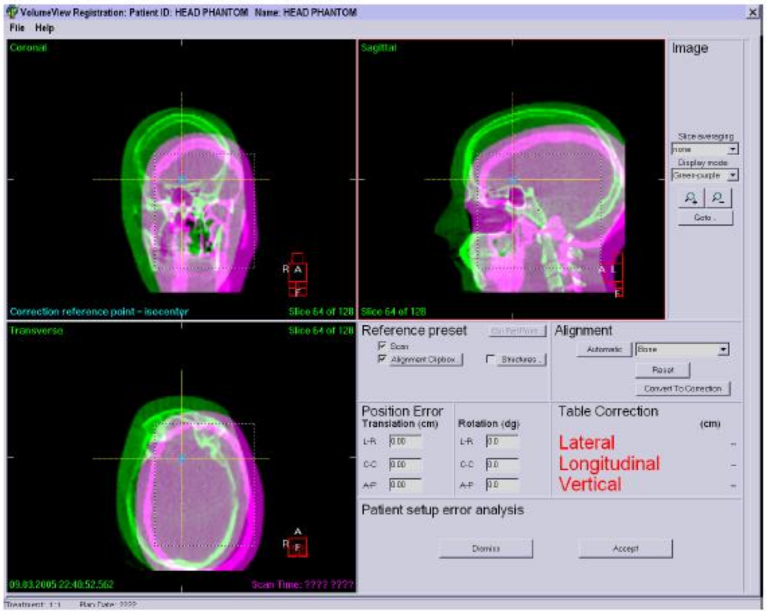

VolumeView Registration: Patient ID: HEAD PHANTOM Name: HEAD PHANTOM

Correction reference point - isocenter

Slice 64 of 128

Slice 64 of 128

Slice 64 of 128

Slice averaging: none

Display mode: Green-purple

☑ Scan

☑ Alignment Clipbox ..

☐ Structures ..

Alignment: Bone

Translation (cm)		Rotation (dg)	
L-R	0.00	L-R	0.0
C-C	0.00	C-C	0.0
A-P	0.00	A-P	0.0

Table Correction	(cm)
Lateral	–
Longitudinal	–
Vertical	–

09.03.2005 22:40:52.562

Scan Time: ???? ????

Treatment: 1:1 Plan Date: ????

Figure 3.7: Screen shot of VolumeView™ image registration. The CBCT image in purple is translated to match to the reference simulation image in green. (Photo courtesy of Elekta, Stockholm, Sweden)

Once the images have been registered the software calculates the necessary translational shifts to align the patient to the linac isocenter. XVI is capable of calculating rotational shifts as well with use of the robotic HexaPOD treatment table (Treatment Intelligence, Schwabmünchen, Germany).[14] The soft tissue contrast and sub-millimeter spatial resolution allow registration to be performed based on the location of the gross tumor volume, target organ, or surrounding soft tissue surrogates. The volumetric acquisition geometry of CBCT as opposed to the slice by slice approach of standard CT results in uniform spatial resolution in the reconstructed image without the limitation of slice thickness on resolution.[9] The capabilities of XVI CBCT for image guidance have been demonstrated by Sharpe et. al. who have shown that the XVI system can relocate the clinical target to within 1 mm of the prescribed location.[15]

3.2 Cone-beam CT Imaging Dose

The imaging dose from three clinical CBCT scan protocols on the Elekta VXI v. 4.2 was measured using a 2D radiochromic film reference dosimetry protocol and humanoid Rando phantom (The Phantom Laboratory, Salem, NY). Table 3.3 lists the scan protocols used in the study and their parameters.

Table 3.3: Clinical CBCT scan protocols on the XVI system.

Name	Collimation	Filter	Energy	mA/Frame	ms/Frame	#Frames	Angle
Head and Neck	S20	F0	100 kV	10	10	361	-100/100
Chest	M20	F1	120 kV	40	40	650	-180/180
Prostate	M10	F1	120 kV	64	40	650	-180/180

The protocol employs XR-QA model GAFCHROMIC™ film (International Specialty Products, Wayne, NJ) and an Epson Expression 10000XL flat-bed document scanner (Seiko Epson Corporation, Suwa, Nagano, Japan). GAFCHROMIC™ film is designed for dose measurements of diagnostic range photons (20-200 kVp) with a dynamic range of 0.1-20 cGy. The film is constructed of two surface layers and two active layers with thicknesses of 5 μm and 25 μm respectively, sandwiched between a clear yellow and an opaque white polyester layer, each 97 μm thick. Figure 3.8 illustrates the structure of the film used in this study (lot number A09160902A).

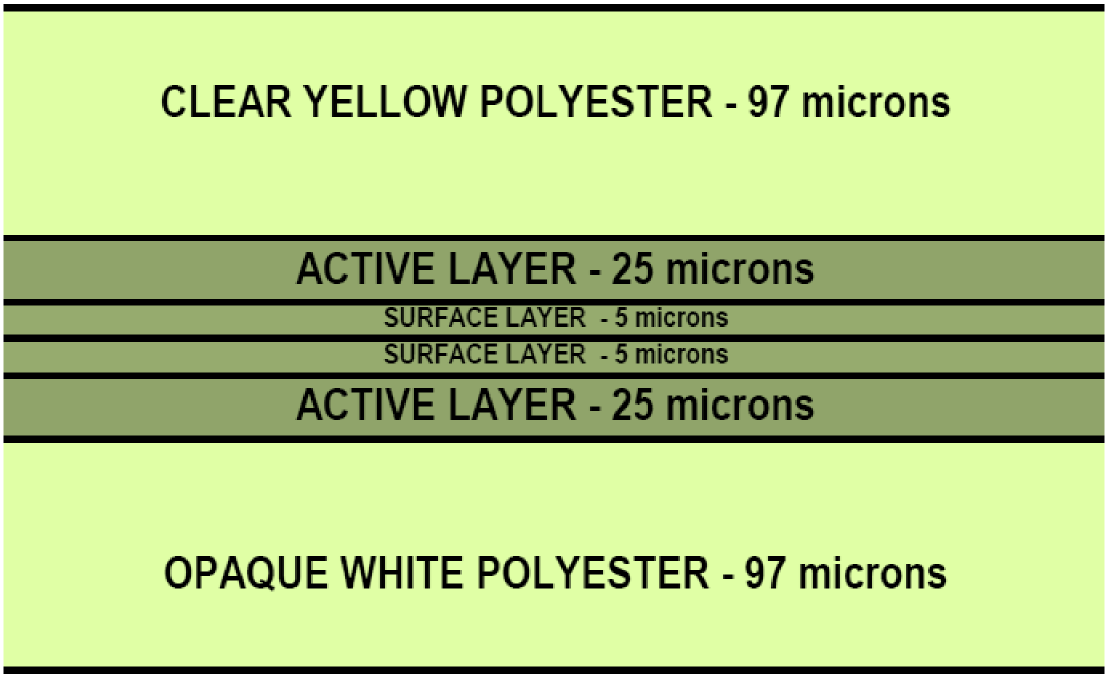

Figure 3.8: Composition of XR-QA GAFCHROMIC™ film.[16]

The active layer nominally consists of H (6.4%), C (38.1%), N (5.5%), O (13.8%), Li(4%), Br (13.4%), and Cs (22.3%) by weight according to the manufacturer. The film requires no processing, can be handled in light, can be cut to fit the application, and develops in real time. Ionizing radiation induces polymerization within the active layer of the film, changing its reflectance and making it appear darker. The darkening of the film is proportional to the radiation exposure it received.[16]

3.2.1 Film Calibration

The response of the film was calibrated in terms of air kerma in air. For both of the beam qualities used in this study (100 kVp F0, 120 kVp F1) the output was measured with a calibrated FLUKE TNT-12000 diagnostic x-ray test device (Fluke Biomedical, Everett, WA) with ion chamber calibration traceable to NIST air kerma standards. The device measures exposure (X) in Röntgens (R), from which air kerma in air was obtained with the following equation:

$$(K_{air}^{film})^{air}[cGy] = 0.876\left[\frac{cGy}{R}\right] \cdot X^{exp}[R] \qquad \text{(Eq. 3.1)}$$

The beam qualities were specified by the first half-value layer measured with the Fluke TNT-12000. To measure HVL, aluminum sheets were placed between the x-ray source and the detector at a distance of 40 cm from the source. To reduce the detection of scatter radiation the detector was placed 40 cm from the attenuating sheets and 80 cm from the source. The narrow beam geometry necessary for accurate measurement of HVL was accomplished by using the M2 collimator with an axial beam width of 3.52 cm at the isocenter. Exposure measurements were taken for increasing thicknesses of attenuator until the signal dropped to half of the initial intensity.

In order to measure the unknown doses from the acquisition of a CBCT scan the film was first calibrated in beams of known kerma. The calibration curve was created by first scanning pieces of film (2 x 4 in.^{2}) with the Epson flat bed scanner in reflection mode. The scanner was set to a resolution of 150 dots per inch in 48 bit RGB mode, and the images saved as tagged image file format (TIFF) files. The films were labelled before scanning for identification purposes. Figure 3.9 is an image of the films before irradiation.

Figure 3.9: XR-QA calibration films pre-irradiation.

For each beam quality ten air kerma points were used for the calibration. The air kerma points ranged from 0 cGy (control film) to 6.0 cGy. For each air kerma point three films were irradiated and the average was found, requiring a total of 30 calibration films per beam quality.

Before irradiating the calibration films the output of the x-ray tube was measured with the FLUKE TNT-12000. The XVI was operated in radiography (static) mode, and the 15x15 collimation cassette was used. The point of measurement of the device was placed at 70 cm from the x-ray source, on the treatment couch. The source to point distance (SPD) was set using the linac optical distance indicator (ODI). The ODI was limited to 75 cm so after setting 75 cm SPD to the device we added 5 cm of solid water to elevate the device to the desired 70 cm SPD. The gantry was rotated to 270°, placing the x-ray source vertically above the measurement device. A series of exposures for each beam quality were measured and the mean output in mR/mAs was found.

For irradiation of the calibration films a custom phantom was used in order to minimize scatter radiation. The phantom consists of two plastic arms on a plastic base, across which two thin strands of monofilament were suspended. The films were placed across the strands and set to 70 cm source to surface distance (SSD), and irradiated using the same 15x15 collimator used for output measurement. During irradiation the TNT detector was placed directly below the calibration film on the base of the phantom. The distance between film and detector amounted to 25 cm. The purpose of the detector was to monitor the output of the tube during irradiation. By assuming the highest delivered kerma point to be known by multiplying measured output (mR/mAs) by the total mAs of the exposure, the rest of the kerma points could then be scaled by the detector reading to obtain the true kerma delivered to each film. Figure 3.10 shows the setup for irradiating the calibration films.

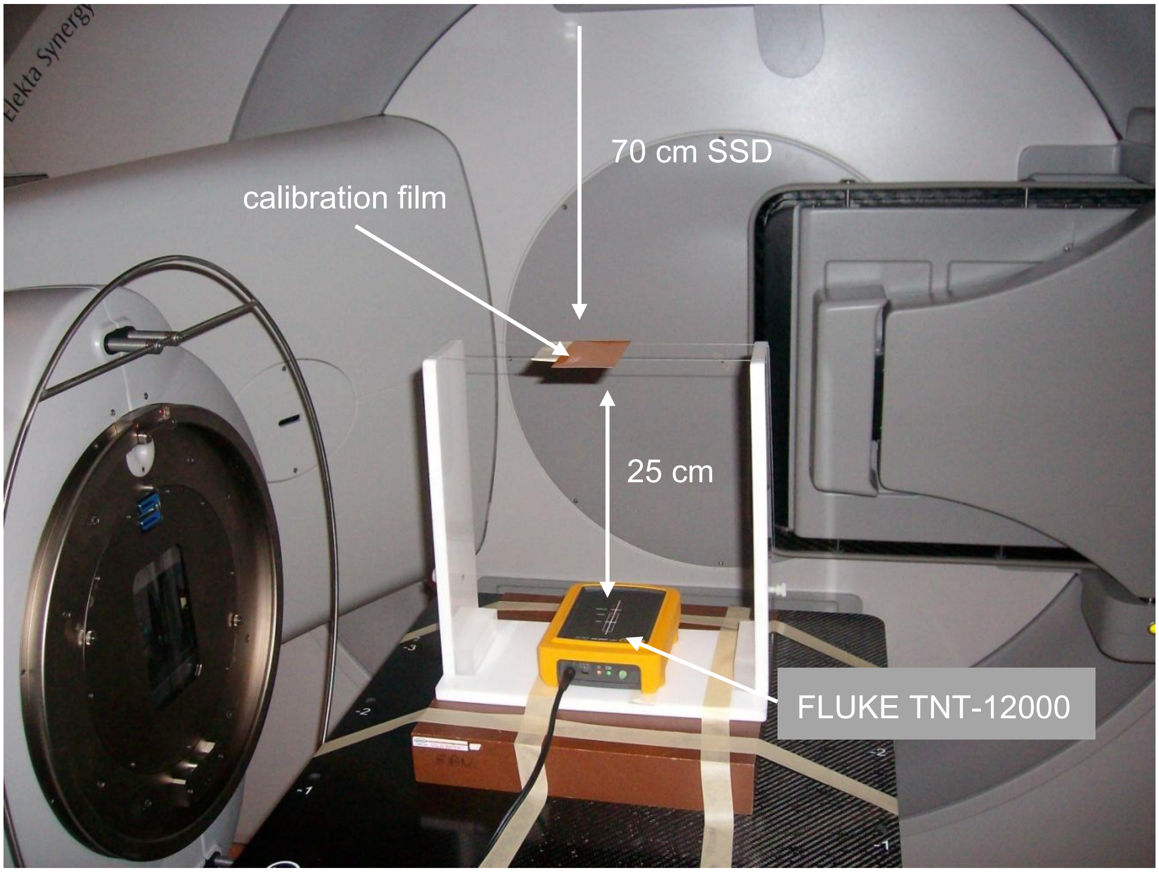

Figure 3.10: Experimental setup for XR-QA film calibration in air.

The irradiated films were scanned 24 hours after exposure. The reflectance of the films (R) was found using an in-house image manipulation script in MATLAB^{TM} (The Math Works Inc., Natick, MA). The routine samples pixels over a

1x1 mm^2 region of the film. To minimize the effect of film non-uniformities (within a single film) on the measured reflectance the films were sampled over the same region before and after irradiation.

XR-QA film has two absorption peaks at 585 nm and 636 nm. The net reflected optical density as a function of wavelength for several doses is given in figure 3.11. The wavelength of the large peak at 636 nm corresponds to the color red in the visible spectrum. To take advantage of this we used the red channel from the scanned image, where the signal is largest.

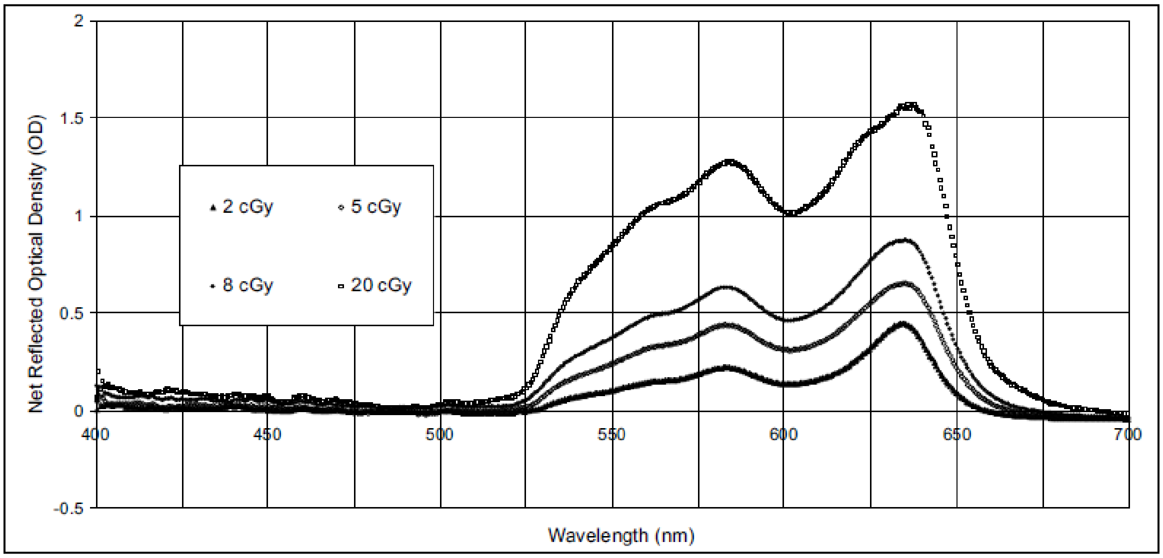

Figure 3.11: Net Absorption of XR-QA film for doses up to 20 cGy.[17]

For every air kerma point, the change in reflectance (ΔR) of each of the three pieces (i) was found as follows: =

$$\Delta R^i = R^i_{before} - R^i_{after} = \frac{1}{2^{16}}\left[PV^i_{before} - PV^i_{after}\right] \quad , \qquad (3.2)$$

where PV represents the 16 bit pixel value from the red channel over the ROI of the saved TIFF image. The uncertainty on the change in reflectance is:

$$\sigma_{\Delta R^i} = \frac{1}{2^{16}} \sqrt{(\sigma(PV^i_{before}))^2 + (\sigma(PV^i_{after}))^2} \tag{3.3}$$

The mean change in reflectance for every air kerma point was found using a weighted mean:

$$\overline{\Delta R} = \sum_{i=1}^{3} (w^i \cdot \Delta R^i) \tag{3.4}$$

The corresponding weights in the averaging equation were calculated as:

$$w^i = \frac{1/(\sigma_{\Delta R^i})^2}{\sum_{i=1}^{3} (1/(\sigma_{\Delta R^i})^2)} \tag{3.5}$$

The corresponding standard deviation on $\overline{\Delta R}$ was calculated as:

$$\sigma_{\overline{\Delta R}} = \sqrt{\frac{1}{\sum_{i=1}^{3} \left(\frac{1}{\sigma_{\Delta R^i}} \right)^2}} \tag{3.6}$$

In order to account for background radiation and environmental effects the change in reflectance of the control (non-irradiated) film was subtracted from the irradiated films to obtain the final reflectance change ($net\Delta R$):

$$net\Delta R = \overline{\Delta R} - \overline{\Delta R_{control}} = M_{film} \quad , \tag{3.7}$$

where M_{film} is used as short notation for the net reflectance change.

The standard deviation on the net change is then given by:

$$\sigma_{net\Delta R} = \sqrt{(\sigma_{\overline{\Delta R}})^2 + (\sigma_{\overline{\Delta R}_{control}})^2} \tag{3.8}$$

The calibration curve for the two beam qualities was created by plotting the kerma points (cGy) as a function of the net change in reflectance. The curves were fit to the data using the following analytical functions: For beam quality with 100 kVp and no bowtie filtration (F0):

$$(K_{air}^{film})^{air} = \frac{a + c \cdot net\Delta R}{1 + b \cdot net\Delta R} \tag{3.9}$$

And for beam quality with120 kVp and additional bowtie filtration (F1):

$$(K_{air}^{film})^{air} = a + b \cdot net\Delta R + c \cdot (net\Delta R)^3 \tag{3.10}$$

The fit functions were chosen based on the following criteria: The function should be monotonically increasing; it should pass through the origin since we expect no response to zero dose (i.e. $a = 0$) ; and it should have the least relative uncertainty for the fitting parameters. Though a single calibration curve for the film would be of convenience, the energy dependence of the film required that for these two beam qualities, and this lot number of film, two curves be used to minimize uncertainty.

The uncertainty in the conversion of net change in reflection into air kerma in air can be found following the work of Devic et. al.[18] using error propagation:

$$\sigma_y^2 = \sum_i \left(\frac{\partial y}{\partial x_i} \right)^2 \cdot \sigma_{x_i}^2 \quad , \tag{3.11}$$

where y represents the total uncertainty of dose measured with the radiochromic film protocol calculated with equation 3.9 or 3.10, x_i includes net reflectance and each of the fit function parameters, and σ_{x_i} are their respective uncertainties. The total uncertainty can then be separated into the experimental uncertainty and the uncertainty in the fitting. For the beam quality 100 kVp F0 the relative experimental uncertainty of the measured air kerma in air for equation 3.9 is:

$$(\sigma_{(K_{air}^{film})^{air}})^{\exp}(\%) = \frac{\left(\frac{c}{(1+b \cdot net\Delta R)^2} \right) \cdot \sigma_{net\Delta R}}{(K_{air}^{film})^{air}} \cdot 100 \quad , \tag{3.12}$$

and the relative fit uncertainty is:

$$(\sigma_{(K_{air}^{film})^{air}})^{fit}(\%) = \frac{\sqrt{\left(\frac{-c \cdot net\Delta R^2}{(1+b \cdot net\Delta R)^2} \right)^2 \cdot \sigma_b^2 + \left(\frac{x}{1+b \cdot net\Delta R} \right)^2 \cdot \sigma_c^2}}{(K_{air}^{film})^{air}} \cdot 100 \tag{3.13}$$

The total uncertainty in the measured air kerma for the fit function of equation 3.9 is given by:

$$(\sigma_{(K_{air}^{film})^{air}})^{total}(\%) = \frac{\sqrt{\left(\frac{-c \cdot net\Delta R^2}{(1+b \cdot net\Delta R)^2} \right)^2 \cdot \sigma_b^2 + \left(\frac{net\Delta R}{1+b \cdot net\Delta R} \right)^2 \cdot \sigma_c^2 + \left(\frac{c}{(1+b \cdot net\Delta R)^2} \right)^2 \cdot \sigma_{net\Delta R}^2}}{(K_{air}^{film})^{air}} \cdot 100 \tag{3.14}$$

The experimental uncertainties are caused by the contribution of $net\Delta R$ measurements which are governed by measurement reproducibility, registration of film images, uncertainties in x-ray tube calibration and reproducibility, temporal and thermal mismatch of films, non-uniformity of response between film pieces, and uncertainties in the image scanning process.

For the beam quality of 120 kVp F1, and the fit function of equation 3.10, the relative experimental uncertainty is given by:

$$(\sigma_{(K_{air}^{film})^{air}})^{\exp}(\%) = \frac{(b + 3c \cdot net\Delta R^2) \cdot \sigma_{net\Delta R}}{(K_{air}^{film})^{air}} \cdot 100 \quad , \tag{3.15}$$

and the relative fit uncertainty is:

$$(\sigma_{(K_{air}^{film})^{air}})^{fit}(\%) = \frac{\sqrt{net\Delta R^2 \cdot \sigma_b^2 + net\Delta R^6 \cdot \sigma_c^2}}{(K_{air}^{film})^{air}} \cdot 100 \tag{3.16}$$

The total relative uncertainty in the measured kerma for the fit function of equation 3.10 is given by:

$$(\sigma_{(K_{air}^{film})^{air}})^{total}(\%) = \frac{\sqrt{net\Delta R^2 \cdot \sigma_b^2 + net\Delta R^6 \cdot \sigma_c^2 + (b + 3c \cdot net\Delta R^2)^2 \cdot \sigma_{net\Delta R}^2}}{(K_{air}^{film})^{air}} \cdot 100 \tag{3.17}$$

After fitting the curve the net change in reflectance can be converted to air kerma in air. The next step is to convert air kerma in air to dose to water.

3.2.2 Dose Conversion

The formalism for converting the air kerma in air measured with film into dose to water at the surface of a phantom is based on the TG-61 protocol with the following equation:

$$D_w = (K_{air}^{film})^{air} \cdot B_w \cdot \left(\frac{\mu_{en}}{\rho}\right)_{air}^{w} , \qquad (3.18)$$

where $(K_{air}^{film})^{air}$ is the air kerma free in air measured with the calibrated radiochromic films, B_w is the backscatter factor, and $\left(\frac{\mu_{en}}{\rho}\right)_{air}^{w}$ is the ratio of the mean mass-energy absorption coefficients water to air. The mean mass-energy absorption coefficients can be found in the TG-61 protocol where they are given as a function of HVL for a certain beam quality. Though TG-61 essentially determines kerma to water at the surface of a phantom, the kerma to water and dose to water are quantitatively equal due to the short electron ranges at this energy and low radiative component of total kerma for low atomic number materials.[18] The backscatter factor B_w corrects the free in air measurement for the effect of photon backscatter that would occur at the surface of a phantom. The backscatter factor is dependent upon knowledge of the exact geometry of the setup including phantom geometry and composition and x-ray field size, SSD, and energy. Rather than attempt to determine the backscatter factor in the clinic, which is discouraged by TG-61[19] for being a non-trivial measurement, this protocol links the film air kerma calibration free in air directly to a film measurement on the surface of the phantom. For each beam quality the air kerma calibration yields a calibration coefficient of the form:

$$N_{K,film} = \frac{K_{air}}{M_{film}} \quad , \tag{3.19}$$

where K_{air} represents the air kerma free in air, and for simplicity replaces the previous notation of $(K_{air}^{film})^{air}$. M_{film} represents the reading of the film system measurement of $net\Delta R$ from equation 3.7. This air kerma calibration coefficient can be converted to a dose to film sensitive-layer calibration coefficient with the following equation:

$$N_{D,film} = \frac{D_{film}}{M_{film}} = \frac{K_{air}(D_{film}/K_{air})_{free-air}}{M_{film}} = N_{film}(D_{film}/K_{air})_{free-air} \quad , \tag{3.20}$$

where $(D_{film}/K_{air})_{free-air}$ represents the ratio of dose to the film sensitive layer to air kerma free in air.

If the range of the secondary electrons is small compared to the thickness of the sensitive layer, this ratio can be approximated by:

$$(D_{film}/K_{air})_{free-air} \cong (K_{film}/K_{air})_{free-air} \cong \left[\left(\frac{\mu_{en}}{\rho}\right)_{air}^{film}\right]_{free-air} \quad , \tag{3.21}$$

where if bremsstrahlung can be ignored, the ratio of kerma to the film sensitive layer to air kerma free in air can be approximated by a mean mass-energy absorption coefficient ratio film to air. Kerma at the surface of the phantom can be found by irradiating the film on the surface of the phantom and applying:

$$K_w = M_{film} \cdot N_{D,film} \cdot (K_w / D_{film})_{surf} \quad , \tag{3.22}$$

where M_{film} represents the film response ($net\Delta R$) measured on the surface of the phantom rather than free in air as before.

If the ranges of the secondary electrons are small compared to the thickness of the XR-QA sensitive layer then the last term can be approximated by:

$$(K_w / D_{film})_{surf} \cong (K_w / K_{film})_{surf} \cong \left[\left(\frac{\mu_{en}}{\rho} \right)^{w}_{film} \right]_{surf} , \tag{3.23}$$

where $\left[\left(\frac{\mu_{en}}{\rho} \right)^{w}_{film} \right]_{surf}$ represents the mean mass-energy absorption coefficient ratio water to film for the spectrum of photons present at the surface of the phantom, which vary from those in air due to the presence of scatter radiation from the presence of the phantom. Substituting equation 3.20 into equation 3.22 allows the determination of water kerma at the surface of the phantom using one of the following equations:

$$K_w = N_{K,film} \cdot M_{film} (D_{film} / K_{air})_{free-air} (K_w / D_{film})_{surf} \tag{3.24}$$

$$K_w = N_{K,film} \cdot M_{film} \left[\left(\frac{\mu_{en}}{\rho} \right)^{film}_{air} \right]_{free-air} \cdot \left[\left(\frac{\mu_{en}}{\rho} \right)^{w}_{film} \right]_{surf} \tag{3.25}$$

This reference radiochromic film dosimetry protocol, developed by Tomic et. al.,[20] presents two conversions. The first (equation 3.24) is termed the full dose-based conversion, and the second (equation 3.25) is termed the kerma-based correction method.

If the film were to be considered completely energy independent then the kerma-based conversion (equation 3.25) could be further approximated with a mean mass-energy absorption coefficient water to air. The resulting equation would be the original TG-61 equation with the air kerma in air and backscatter factor terms replaced by a single on-phantom-surface kerma measurement taken with film. This combined with the mean mass-energy absorption coefficient ratio easily found in TG-61 would provide a means to accurately measure dose. However, the significant high atomic number constituents of XR-QA model GAFCHROMIC™ film means that it is considerably energy dependent and that the assumptions made to simplify the conversion are not trivial. The authors therefore investigated the difference between a complete Monte Carlo evaluation as in equation 3.24 and a simple spectrum averaged $\left(\frac{\mu_{en}}{\rho}\right)_{air}^{w}$ approximation as in the kerma-based conversion (equation 3.25). The investigation found that for five different x-ray beam qualities the difference between the full dose-based conversion and the kerma-based conversion was less than 1% and can be ignored in diagnostic applications allowing use of the following equation for accurate dosimetry of kV beams:

$$D_w = K_w = (K_{air}^{film})^w \cdot \left(\frac{\mu_{en}}{\rho} \right)_{air}^{w} \tag{3.26}$$

We used equation 3.26 for the calculation of CBCT imaging dose in this study.

3.2.3 Scan Acquisition

The dose from XVI CBCT scans was measured in-vivo using a humanoid Rando phantom (The Phantom Laboratory, Salem, NY) as a patient surrogate. The Rando phantom used was the male version which simulates a 175 cm tall, 73.5 kg man. The phantom is constructed of a proprietary urethane which has the same absorption properties as human flesh at radiotherapy energies, and mimics muscle tissue with randomly distributed fat. Lung simulating material is present in the thorax within the ribcage, with the same effective atomic number of the soft tissue material with a physical density that mimics human lungs in the median respiratory state. The phantom also contains a skeletal structure of authentic human bone. To enable dose measurement with the phantom it is cut into 2.5 cm thick axial slices which make it readily usable for film dosimetry.[21]

Figure 3.12: Thorax region of Rando phantom with skin dose films taped to the surface.

Dose measurements were performed in the head and neck, thorax, and pelvis regions. The CBCT scan protocols used where those listed in table 3.3; each being used in conjunction with the appropriate anatomical region. Two aspects of patient dose were investigated: Point skin doses in the left, right, anterior, and posterior aspects; and dose profiles through the patient in the left-right and anterior-posterior orientations.

The films for the dose profiles were cut from the same lot number as the calibration films. The profile films were cut 1” wide with the length determined by the dimensions of the phantom in the region of interest. Each film was sandwiched between two slices of the phantom in the regions of interest. The left-right (LAT) and anterior-posterior (VERT) profile films were separated by one phantom slice to eliminate changes in secondary particle fluence that would result if they were to be in contact.

The skin dose films were cut into 1” x 2” pieces and affixed to the left, right, anterior, and posterior aspects of the phantom in the region of interest using paper tape. Each region then had six films: two profile films and four skin dose films. Each unique film cut (LAT, VERT, skin) for each region was also accompanied by a control film. Each measurement was performed three times with new film in place for every scan acquisition. Scans that faulted or stopped prior to completion were rejected, and new films loaded into the phantom for repetition of the scan.

3.2.4 Film Analysis

Prior to irradiation all films were scanned in the Epson 10000XL flat-bed document scanner, and then again 24 hours post-irradiation to reduce the effects on calculated dose of temporal mismatch between the calibration films and the measurement films. The films were scanned both times in the same orientation, and within the region of the scanner which had been previously determined to be the most uniform in sensitivity. For organizational purposes the films were labelled and the scanned images grouped by anatomical region and aspect, as illustrated in figure 3.13.

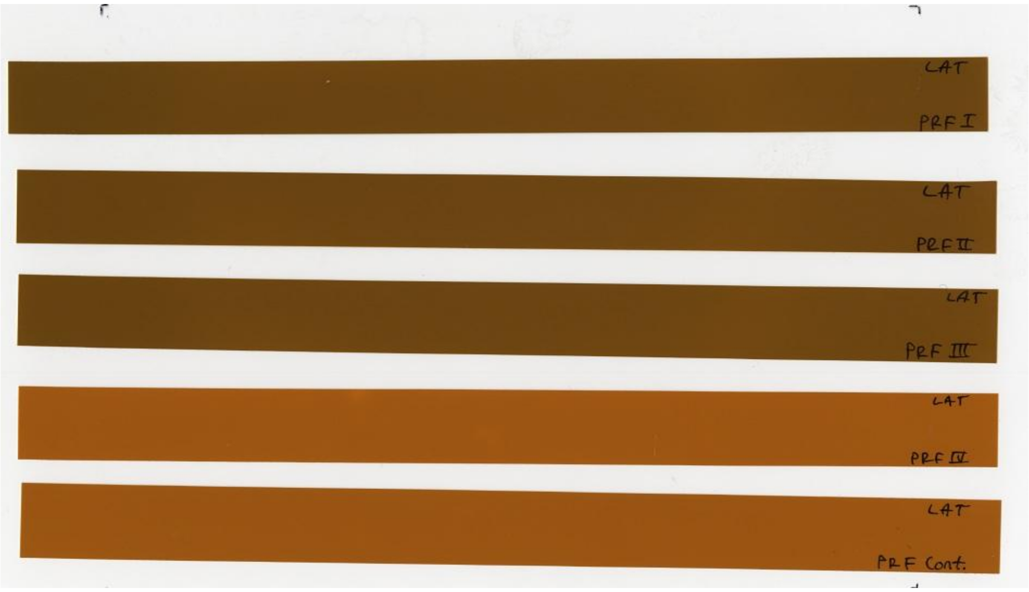

Figure 3.13: XR-QA film strips used to measure lateral dose profiles in the pelvic region. The irradiated films are noticeably darker.

The TIFF files were analyzed in an in-house script written in MATLAB, where the 16 bit deep pixel values were found for the calibration films, skin dose films, profile films, and control films. For the skin dose and calibration films a region of interest 1 mm x 1 mm was sampled in the script and the mean pixel value and standard deviation reported. For the profile films it was necessary to first align the film vertically for registration with the control film. After alignment the strip of pixels straight down the center of the film from top to bottom was sampled and the mean value at each point and standard deviation were reported. With the reported pixel value data from MATLAB the formalism presented previously was applied to find the dose to the patient from acquisition of the three CBCT scan protocols.

3.3 Dose Calculation with CBCT Data Sets

CBCT images are typically used for daily image guidance. With recent advances in adaptive radiotherapy, treatment protocols can involve replanning for cases where significant anatomical changes have taken place (e.g. weight loss, tumor shrinking). In these cases it would be advantageous to replan treatments using the already on-hand CBCT data sets from daily IGRT. The use of CBCT images for replanning would reduce the total patient imaging dose and lighten the clinical workload. There are studies in the current literature on the feasibility of on-line planning and delivery using CBCT image sets.[22]

Current treatment planning techniques involve the use of heterogeneity corrections to correct the dose calculation for the non-uniform densities through which treatment beams pass. It has been shown that uncorrected plans can lead to radiation dose errors in excess of 30% of the intended dose.[23,24] To correct for heterogeneities, the treatment planning system needs information of the density of each voxel through which the beam passes. The reconstructed CT image displays the 3D model of the patient as a map of voxels whose voxel or pixel gray value, which is proportional to CT number in Hounsfield units (HU), is representative of the density of the imaged material at that point. The CT number is determined using the equation[1]:

$$CT\ number\ [HU] = K\left(\frac{\mu}{\mu_{H20}} - 1\right)\ . \tag{3.26}$$

The constant K is chosen by the vendor, and this equation is representative of what is generally used for calculation of CT number though vendors may make small changes which must be taken into account for a complete understanding. To obtain density information from CT number the treatment planning system needs a CT number to density calibration (CT-D). Measured CT numbers for a given material can vary from system to system; therefore it is necessary to create a CT-D for each imager in use.[25]

3.3.1 Calibration of the Hounsfield Unit

3.3.1.1 Simulation CT Calibration

Calibration of the Hounsfield unit for the CT simulator can be accomplished using commercially available density phantoms including Catphan (The Phantom Laboratory, Salem, NY) and CIRS model 62 density phantom (CIRS Tissue Simulation Technology, Norfolk, VA).

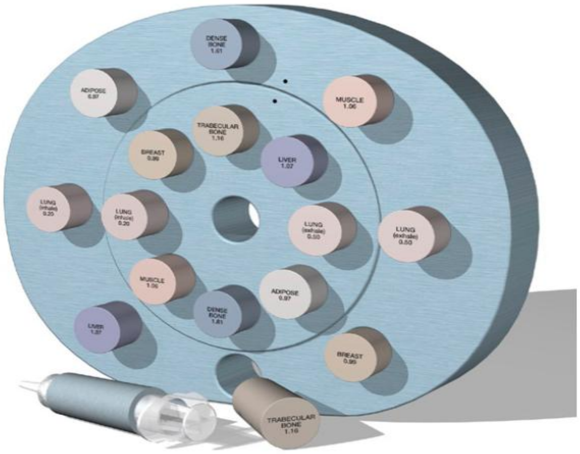

Figure 3.14: CIRS Model 62 density phantom (CIRS Tissue Simulation Technology, Norfolk, VA).[26]

The CIRS model 62 contains density inserts of different materials with known densities which simulate various tissues ranging from lung to trabecular bone. There are six steps to the calibration:

1. Scan the phantom in the CT simulator
2. Export the image set to the treatment planning system
3. Create regions of interest (ROI) within each density insert
4. Plot the reported mean CT number of each insert against the known density
5. Fit the data to a bilinear function
6. Save simulator CT-D curve (CT-$D_{sim)}$ for use when planning treatments with images from this simulator

The CT number calculation will vary for a given imager based on energy, so a CT-D_{sim} must be created for each energy. The first piece of the bilinear function should cover the region from -1000 HU (air) to 0 HU (water), and the second piece from 0 HU to the highest point.[25] The treatment planning system (TPS) used in this study was the Pinnacle^3 system (Pinnacle v. 8.0m, Phillips Healthcare, Andover, MA). The Pinnacle TPS shifts the CT number data by +1000 so that the nominal CT number of air is 0 HU and that of water is 1000 HU. The fitted bilinear function will be used by the TPS to interpolate between density points.

3.3.1.2 CBCT

The key issue with CBCT images in respect to dose calculation is the effect of scatter on calculation of CT number. The large scatter contribution in the reconstructed image prevents a direct correlation of pixel value to CT number. This in itself is not an overwhelming problem, for even a very poor calculation of CT number can be corrected with a well constructed CT-D curve. The problem arises when the effect of object geometry on calculation of CT number is studied. The lack of physical scatter rejection options and the combination of large fields and large detector area give rise to a situation where the amount of scatter, and therefore the CT number calculated in the reconstruction, vary significantly with object size and beam geometry. This is in opposition to the fan-beam geometry of the CT simulator whose small slice width and scatter rejection grid eliminate nearly all dependence upon object geometry. Hatton et. al.[27] studied the effect of phantom geometry on CT number and found that:

- Increasing axial length of the phantom by 5 cm led to a change in CT number of 260 HU for a high density insert.
- Increasing phantom diameter from 18 to 40 cm led to a change in CT number of up to 1200 HU for a high density insert.

Thus the use of a CT-D curve made for one phantom will not be accurate for use with another of different size, or a patient of different size. The change in scatter contribution for different FOV and axial length values will render CT-D curves made from one protocol inaccurate for use with an image scanned with a different protocol. These large errors in CT number calculation lead to errors in determination of density, and from there to errors in calculation of dose. Parker et. al.[28] found that a 5% error in determination of density will lead to a 1% error in dose calculation, meaning that a 1200 HU error can lead to a very large error in calculated dose.

This study sought to evaluate the ability to calculate dose based on CBCT images. The effect of scatter on the calibration of the HU was corrected by creating CT-D curves using three methods: density phantom method, patient specific method, and CT simulator method. The obtained results were compared to CT simulator image based results.

3.3.1.2.1 Density Phantom Method

This method corrects for scatter by creating a CT-D curve using a CIRS model 62 density phantom and the same six step technique discussed in section 3.3.1.1. The effect of the beam geometry of a given protocol on CT number calculation is accounted for by creating a CT-D curve specific to a given scan protocol. This protocol-specific CT-D curve (CT-D_{M15F1}) is used for dose calculations in Pinnacle only for patients scanned with the same protocol (all parameters are constant). This method corrects for the effect of beam geometry on scatter, but cannot correct for the effect of object geometry.

3.3.1.2.1 Patient Specific Method

This method, proposed by Richter et. al.[29], corrects for both beam geometry and object geometry. The CT-D curve is made by investigating similar regions within the patient in both the planning CT and image guidance CBCT image sets. Instead of using a phantom with known density inserts to populate the CT-D table, the patient's own anatomy is used. ROI's are drawn within fat, muscle, bladder, bone, etc., on the CBCT image and in the CT image as well.

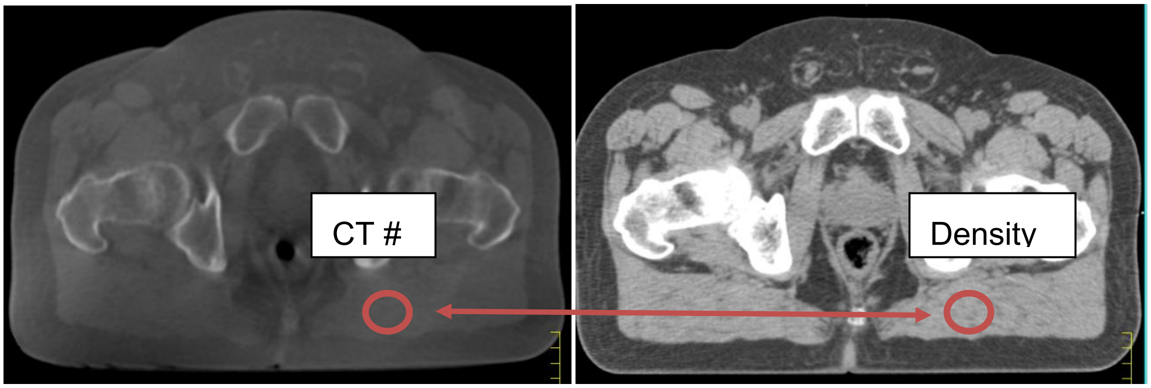

Figure 3.15: Correlation of CT # and density for patient specific method.

From the CBCT image the mean CT numbers are reported, and these are plotted against the ROI density reported in the CT image. The densities reported in the CT image are calculated using the reported mean CT number and CT-D_{sim} from commissioning of the imager. This method creates a scenario where the patient and the “phantom” share the same geometry. The created calibration curve (CT-$D_{patient}$) is used to calculate dose in Pinnacle for the patient it was created from.

3.3.1.2.2 CT Simulator Method

This method uses CT-D_{sim} , the same as created for the CT simulator using the density phantom. There is no correction for scatter in this method; it is used as a baseline to evaluate the improvement on dose calculation provided by the protocol-specific and patient-specific methods.

In order to evaluate these methods treatment plans created in the Pinnacle TPS were applied to both CBCT image sets and CT image sets. Dose was calculated using the adaptive convolve algorithm with heterogeneous beam computation and the resulting dose calculated from CBCT images and CT images were compared. Two treatment sites were evaluated: Prostate and spine.

3.3.2 Prostate Case

To compare dose calculation in CBCT image sets to CT image sets, the beams from the original treatment plan of a prostate patient were imported into the

CBCT image set. The CBCT image set was acquired from the XVI station from the saved records of the patient's daily CBCT IGRT.

The prostate, bladder, rectum, seminal vesicles, and femoral heads were contoured in the CBCT image set. The contouring was done by hand, and with no regard for the volume or position of the contours in the CT image.

The treatment beams were attached to the isocenter of the CBCT image. To ensure that the beams had the same isocenter in the patient for each plan, the isocenter was registered from the CT image to the CBCT image. The original treatment plan for the patient, an intensity-modulated radiotherapy (IMRT) plan, consisted of 7 beams, 45 multi-leaf collimator (MLC) segments, and 517 monitor units (MU), with a prescribed dose of 180 cGy to the 99% isodose line of the point dose to the isocenter. The dose for each plan (CT and CBCT) was calculated with heterogeneity corrections using the adaptive convolve algorithm. The resulting dose-volume histograms (DVH) were compared.

The position and volume of the prostate, bladder, and rectum vary due to differential bladder and rectum filling, and swelling or shrinking of the prostate due to radiation or hormone therapy. This variation makes comparison of the two image sets less than ideal; the DVH is not only affected by the CT-D calibration curve under investigation, but now also by anatomical variation between the original CT and the daily CBCT. To eliminate this anatomical error, this comparison was also performed for a humanoid Rando phantom. The same process of creating an IMRT plan on the CT image set and exporting these beams into the CBCT image set was used. Simulated prostate, bladder, and rectum were contoured in the CT image and the contours registered to the CBCT image. DVHs for the contoured ROIs were evaluated. The rigid anatomy of the phantom allows a more direct comparison of dosimetric accuracy of CBCT images.

3.3.3 Spine Case

Of particular interest in radiation therapy is on-line treatment planning using CBCT. For the case of emergency spine patients, whose treatment is often palliative, it would be of benefit if the imaging, planning, and delivery could be accomplished without moving the patient from the treatment couch. The dosimetric accuracy of CBCT data sets for calculating dose to the spine and surrounding anatomy was investigated by comparing CBCT calculated dose to CT calculated.

For the emergency spine case, the plan was created in opposite order from the prostate case. Here the treatment was planned on the CBCT image of the patient. The goal of the treatment was to deliver a therapeutic dose to the spine while keeping high isodose lines off of the spinal cord. Two beams (AP-PA) were used with a wedge for the AP beam. The beams, with MU locked, from this plan were then imported into the CT image of the same patient and attached to the isocenter in the same orientation as the CBCT plan. The resulting dose distribution in the CT image was compared to that in the CBCT image. Again, to eliminate the effects of anatomical variations between imaging, the same procedure was applied to the thorax region of the Rando phantom.

References for chapter 3:

1. Wolbarst, A. B.; Physics of Radiology. Medical Physics Publishing, 2005.
2. XVI v. 4.2 Clinical Users Manual.
3. X-ray Production and Imaging Course, Elekta Limited, 2008.
4. Corrective Maintenance Manual for XVI, Elekta Limited 2008.
5. Graham, S.A.; Moseley, D.J.; Siewerdsen, J.H.; Jaffray, D.A.; Compensators for Dose and Scatter Management in Cone-beam Computed Tomography. *Med. Phys.* **34**: 2691-2703, 2007.
6. Siewerdsen, J.H.; Jaffray, D.A.; Optimization of X-ray Imaging Geometry (With Specific Application to Flat-panel Cone-beam Computed Tomography). *Med. Phys.* **27**: 1903-1914, 2000.
7. Jaffray, D.A.; Siewerdsen, J.H.; Cone-beam Computed Tomography with a Flat-panel Imager: Initial Performance Characterization. *Med. Phys.* **27**: 1311-1323, 2000.
8. Private conversation with Zach Reed (Service Engineer, Elekta), October 2009.
9. Jaffray, D.A.; Siewerdsen, J.H.; Wong, J.W.; Martinez, A.A.; Flat-panel Cone-beam Computed Tomography for Image-Guided Radiation Therapy. *Int. J. Radiation Oncology Biol. Phys.* **53**: 1337-1349, 2002.

10. Thorsten M. Buzug; “Computed Tomography: From Photon Statistics to Modern Cone-Beam CT.” (Springer 2008), pp. 30.
11. Feldkamp, L.A.; Davis, L.C.; Kress, J.W.; Practical Cone-Beam Algorithm. *J. Opt. Soc. Am. A* **1**:612-619, 1984.
12. Remeijer et.al.; First clinical experience with Cone-beam CT based setup correction protocols. *Proceedings of the 8th International Workshop on Electronic Portal Imaging*, EPI2K4, 88-89, 92-93.
13. Aubry, J.; Cheung, J.; Pouliot, J.; et. al.; Investigation of geometric distortions on magnetic resonance and cone beam computed tomography images used for planning and verification of high-dose rate brachytherapy cervical cancer treatment. *Brachytherapy* **9**:266-273, 2010.
14. Meyer, J.; Wilbert, J.; Baier, K.; et. al.; Positioning accuracy of cone-beam computed tomography in combination with a hexapod robot treatment table. *Int. J. Radiat. Oncol. Biol. Phys.* **67**: 1220-1228, 2007.
15. Sharpe, M.B.; Moseley, D.J.; Purdie, T.G.; Islam, M.; Siewerdsen, J.H.; Jaffray, D.A.; The stability of mechanical calibration for a kV cone beam computed tomography system integrated with linear accelerator. *Med. Phys.* **33**: 136-144, 2006.
16. International Specialty Products, XR-QA GAFCHROMIC™ Marketing Material.

17. Alnawaf, H.; Cheung, T.; Butson, M.J.; Yu, P.K.N.; Absorption spectra response of XRQA radiochromic film to x-ray radiation. *Radiation Meaurements* **45:**129-132, 2010.

18. Devic, S.; Seuntjens, J; Sham, E.; Podgorsak, E.; Precise radiochromic film dosimetry using a flat bed document scanner. *Med. Phys.* **32:** 2245-2253, 2005

19. Ma, C.M.; Coffey, C.W.; DeWard, L.A.; Liu, C.; Nath, R.; Seltzer, S.M.; Seuntjens, J.P.; AAPM protocol for 40-300 kV x-ray beam dosimetry in radiotherapy and radiobiology. *Med. Phys.* **28**: 868-893, 2001

20. Tomic, N.; Devic, S.; DeBlois, F.; Seuntjens, J.; Reference radiochromic film dosimetry in kilovoltage photon beams during CBCT image acquisition. *Med. Phys.* **37:**1083-1092, 2010.

21. Technical Data Sheet for Rando Phantom. The Phantom Laboratory, Salem, NY.

22. Létourneau, D.; Wong, R.; Moseley, D.; et. al.; Online planning and delivery technique for radiotherapy of spinal metastases using cone-beam CT: image quality and system performance. *Int. J. Radiat. Oncol. Biol. Phys.* **67**: 1229-1237, 2007.

23. Constantinou, C.; Harrington, J.C.; An electron density calibration phantom for CT-based treatment planning computers. *Int. J. Radiat. Oncol. Biol. Phys.* **41**: 787-794, 1992.

24. Mackie, T.R.; El-Khatib, E.; Battista, J.; et. al.; Lung dose corrections for 6 and 15 MV X-rays. *Med. Phys.* **12**: 327, 1985.

25. Saw, C.B.; Loper, A.; Komanduri, K.; et. al.; Determination of CT-to-density conversion relationship for image-based treatment planning systems. *Med. Dos.* **30**: 145-148, 2005.

26. Technical Paper, CIRS Model 62 density phantom. CIRS Tissue Simulation Technology, Forfolk, VA.

27. Hatton, J.; McCurdy, B.; Greer, P.B.; Cone beam computerized tomography: the effect of calibration of the Hounsfield unit number to electron density on dose calculation accuracy for adaptive radiation therapy. *Phys. Med. Biol.* **54**: N329-N346, 2009.

28. Parker, R.P.; Hobday, P.A.; Cassell, K.J.; The direct use of CT number in radiotherapy dosage calculations for inhomogeneous media. *Phys. Med. Biol.* **24**: 802-809, 1979.

29. Richter, A.; Qiaoqiao, H.; Steglich, D.; et. al.; Investigation of the usability of conebeam CT data sets for dose calculation. *Radiation Oncology* **3**: 2008.

Chapter 4: Results and Discussion

4.1 CBCT Imaging Dose

The measured response of a radiochromic film dosimetry system to ionizing radiation is dependent upon three components:

1. Protocol
2. Scanner
3. Film

The aspects of the protocol including the cutting of the film, the way it is scanned, the time between irradiation and scan, and the method for calculation of ΔR from pixel value all affect the measured change in the film, and by extension the measured dose.

The scanner performance and sensitivity of the radiochromic film dosimetry system will necessarily vary by the scanner model and even serial number. The difference in the scanner model comes from a difference in the optical geometry of the scanner, type of the light source used and type of the CCD array employed. All of these three components may also vary between different scanners of the same model.

The film will respond differently for varying photon energy, between film models, batch numbers, and within a single batch. The measured ΔR is not then an objective value, but rather is dependent upon the many variables within a radiochromic film dosimetry system.[1] The calibration of the GAFCHROMIC™ XR-QA film in this study followed the method presented in chapter 4, the results of which are given here.

4.1.1 Film Calibration and Uncertainty Analysis

The output of the x-ray tube for the beam quality of 100 kVp F0 was measured with the TNT-12000 to be 10.53 mR/mAs. This output factor was used at the 6 cGy kerma point to relate the given kerma to the measured reading of the monitor chamber. From this the monitor chamber reading was used to find the actual kerma delivered to each of the calibration films. The measured air kerma as a function of net change in reflectance was then found by converting from exposure to kerma via equation 3.1. The obtained film response as a function of exposure is presented in figure 4.1 (for beam quality 100 kVp F0) and in figure 4.2 (for beam quality 120 kVp F1).

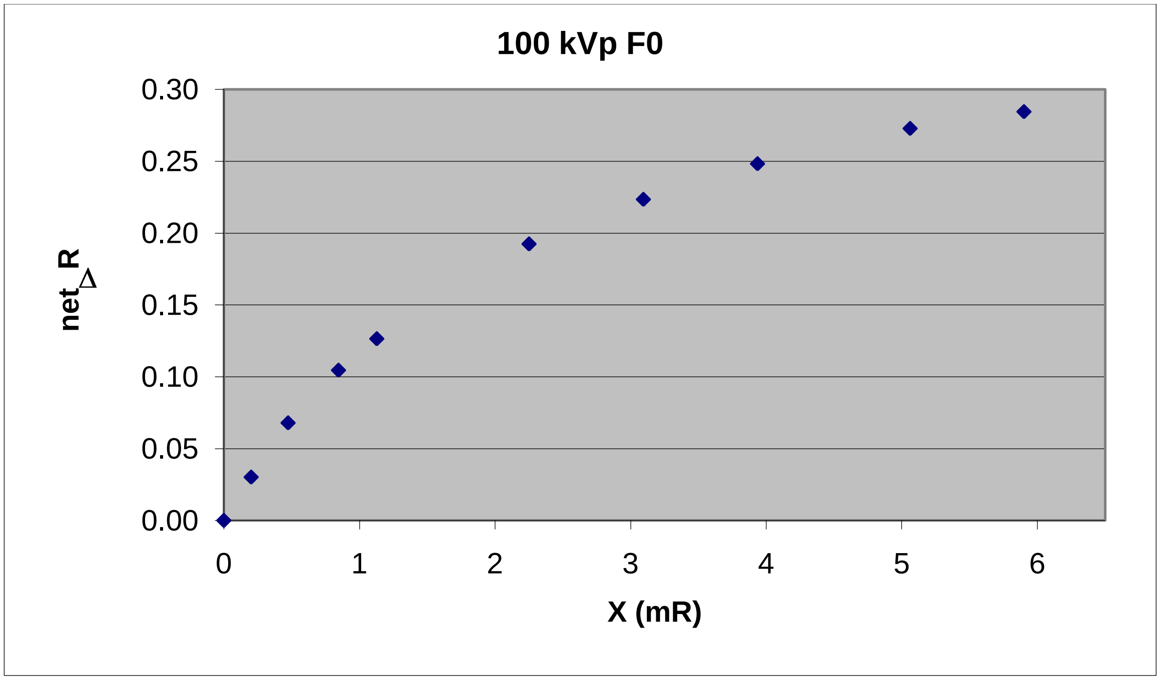

Figure 4.1: Film response as a function of exposure for 100 kVp FO beam quality.

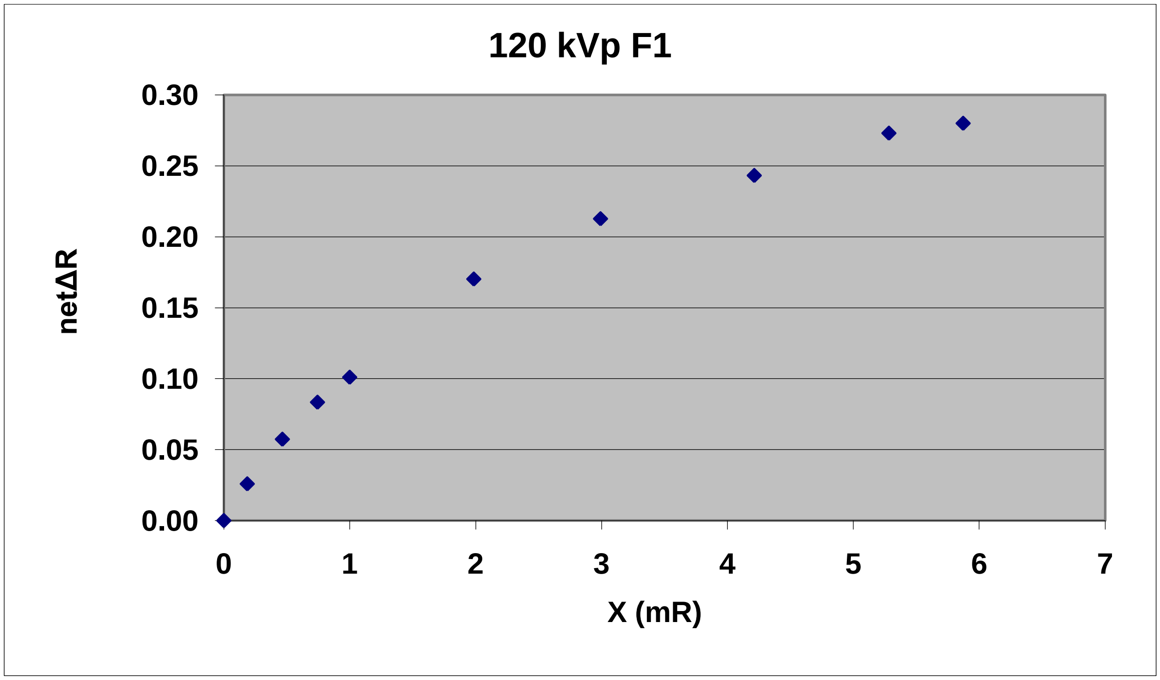

Figure 4.2: Film response as a function of exposure for 120 kVp F1 beam quality.

The obtained fitted calibration curve for the 100 kVp F0 beam quality used in clinical CBCT protocols on XVI (figure 4.3) is obtained using fitted functions described with equation 3.9 in section 3.2.1. For the beam quality of 120 kVp F1 (figure 4.4) the fitted function described with equation 3.10 in section 3.2.1 was used. The fitting parameters are presented in table 4.1.

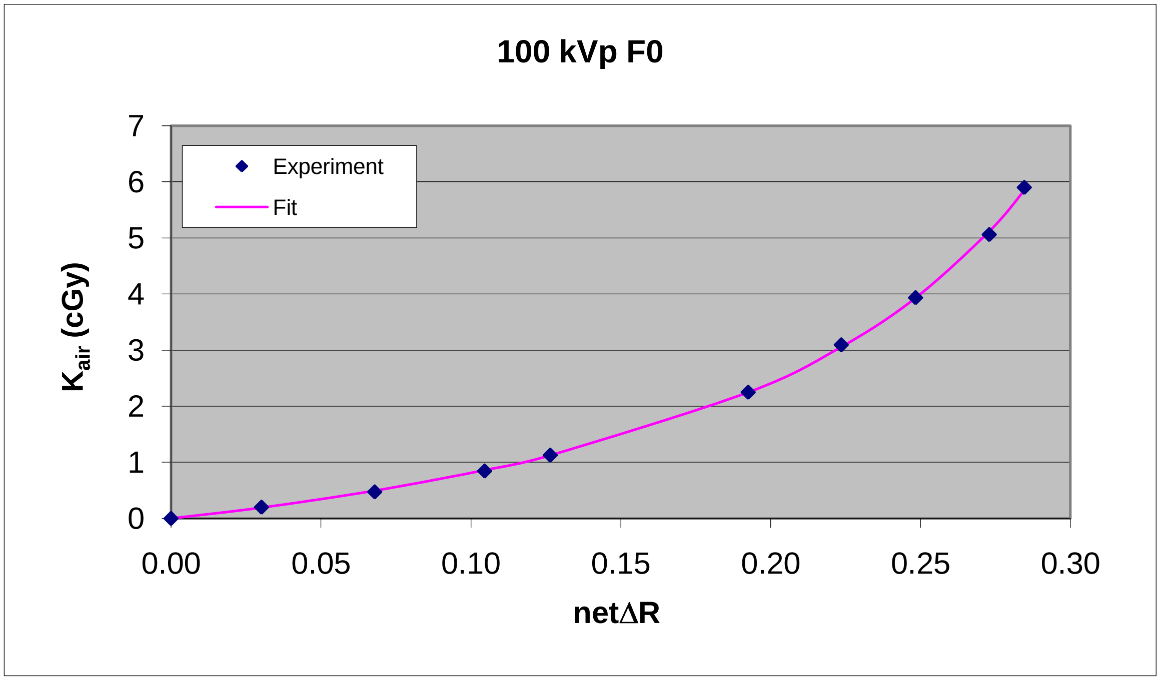

Figure 4.3: Air kerma in air as a function of net change in reflectance for 100 kVp F0 beam quality. Solid line represents the fitted curve.

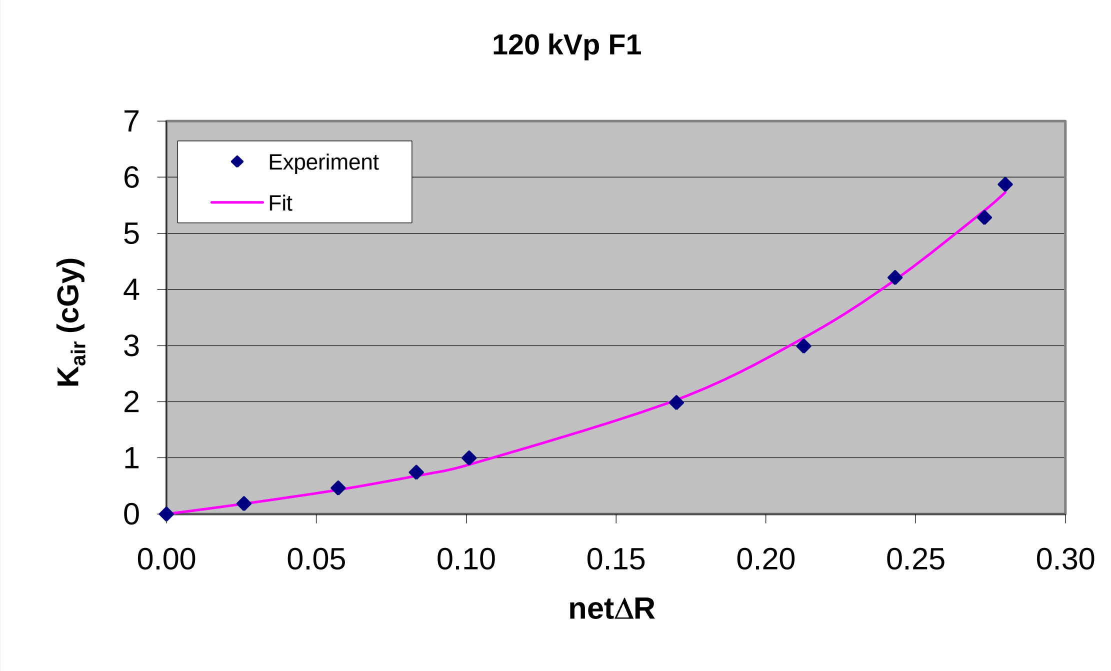

Figure 4.4: Air kerma in air as a function of net change in reflectance for 120 kVp F1 beam quality. Solid line represents the fitted curve.

The fit for each beam quality (table 4.1) has a coefficient of determination (R^2) greater than 0.99. The standard deviation of the fit function parameters contribute to the total uncertainty in measured dose according to equations 3.14 and 3.17

Table 4.1: Fit function parameters.

Beam Quality	Parameter	Value	Standard Deviation	R^2
100 kVp F0	b	-2.46021644	0.03925239	0.999842639
	c	6.195339329	0.23716595	
120 kVp F1	b	6.958141308	0.543601553	0.998005161
	c	172.2847174	8.686176559	

The total uncertainties of the calibration curves are calculated using equations 3.14 and 3.17 in section 3.2.1 and the obtained results are presented in figures 4.5 and 4.6 for corresponding beam qualities 100 kVp F0 and 120 kVp F1.

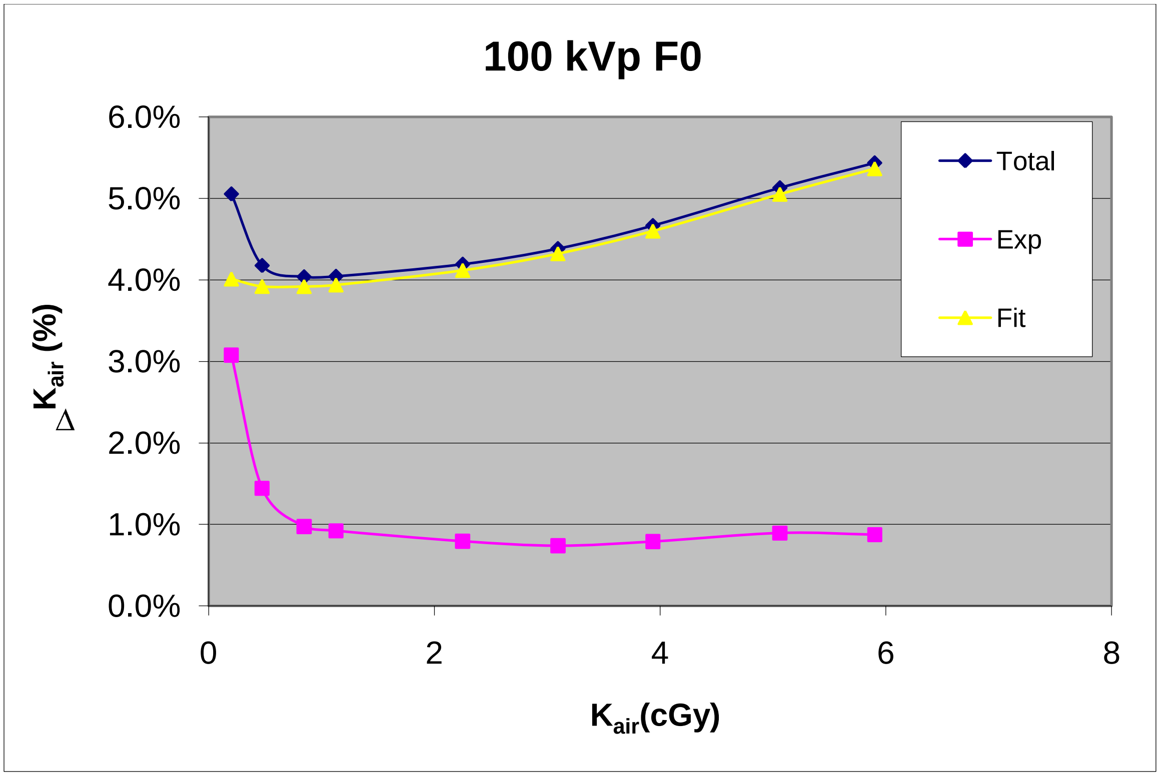

Figure 4.5: Experimental, fit, and total uncertainty as a function of air kerma for the 100 kVp F0 beam quality.

The uncertainty for the calibration curve used for beam quality 100 kVp F0 (figure 4.5) is initially at a maximum and quickly decreases. The experimental uncertainty stays roughly constant as kerma increases, but the total uncertainty increases with kerma as the fit uncertainty increases. In many cases this increase in uncertainty would be undesirable, however in this case the measured doses for the head and neck protocol which utilizes the 100 kVp F0 beam quality are of the order of mGy, where uncertainty is still low. The highest uncertainty is less than 6% which is acceptable for diagnostic range photon beams.

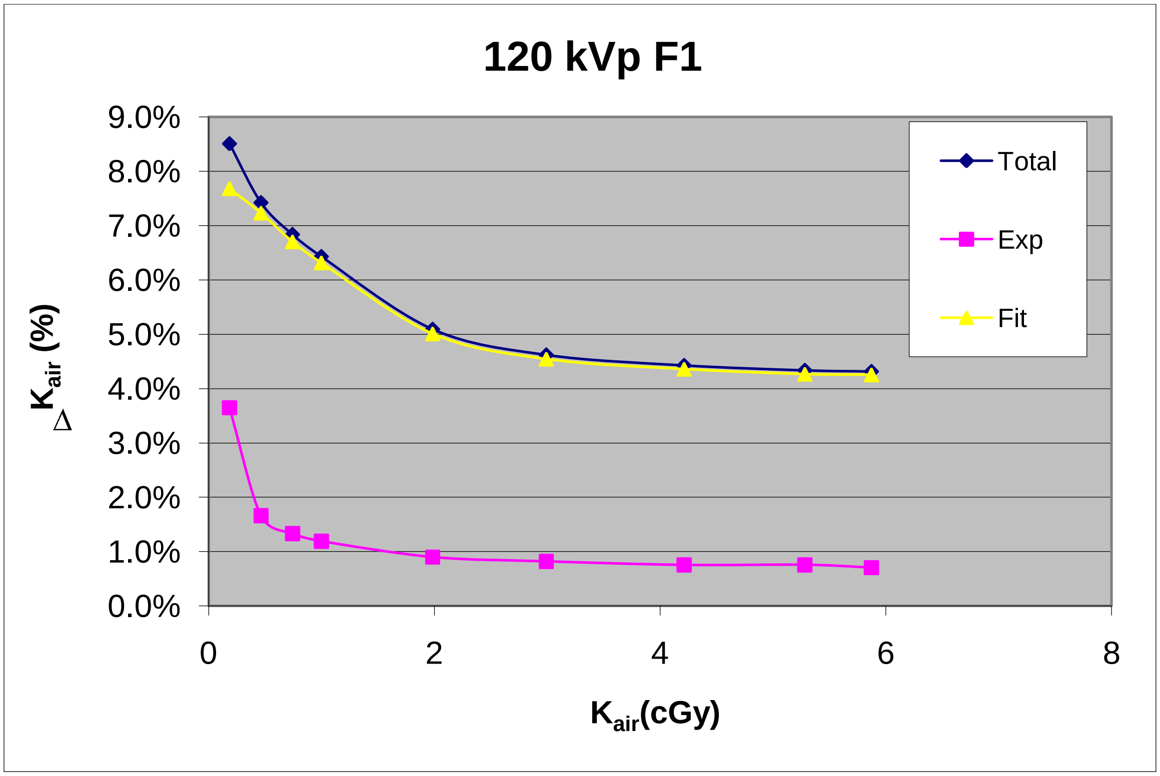

Figure 4.6: Experimental, fit, and total uncertainty as a function of air kerma for the 120 kVp F1 beam quality.

The total uncertainty for 120 kVp F1 beam quality decreases with increasing dose. Although the uncertainty is high for very low doses, the uncertainty for the range of dose measured in this beam quality is below 5%.

4.1.2 Skin Dose

Point skin doses were measured with 1” x 2” strips of film taped on the Rando phantom in the anterior (ANT), posterior (POST), left lateral (LLAT), and right lateral (RLAT) aspects for each of the three protocols. The obtained skin doses together with their corresponding uncertainties are presented in table 4.2

Table 4.2: Skin dose in the ANT, POST, LLAT, and RLAT aspects for three clinical CBCT scan protocols.

Protocol	ANT Surface Dose (cGy)	POST Surface Dose (cGy)	LLAT Surface Dose (cGy)	RLAT Surface Dose (cGy)
Head and Neck S20F0	0.115 ± 0.002	0.108 ± 0.002	0.158 ± 0.003	0.044 ± 0.001
Chest M20 F1	2.5 ± 0.1	2.9 ± 0.1	2.2 ± 0.1	2.5 ± 0.1
Prostate M10 F1	4.5 ± 0.2	3.1 ± 0.1	3.3 ± 0.2	4.0 ± 0.2

The inter-protocol skin doses reported are proportional to the total mAs, with the highest dose in the anterior aspect of the Prostate M10 F1, and the lowest dose in the right lateral aspect of the Head and Neck S20 F0 protocol. The proportionality of dose to mAs is in agreement with results from Song et. al. who found dose during CBCT scans to be linearly proportional to mAs.[2]

The skin doses for the four aspects in the chest protocol are roughly equivalent, as they are for the prostate protocol. For the head and neck protocol, however, there is a large difference between the four aspects. Whereas the gantry sweep is a full 360° for the half-fan geometry, the sweep in the full-fan geometry of the Head and Neck S20 F0 scan is 200°. The x-ray source sweeps symmetrically about the left aspect of the patient; starting at -10° and rotating to 100°. The x-ray source spends the most time in the left aspect of the patient and the least in the right aspect. The dosimetric effect of this asymmetry is apparent in the measured skin dose. The dose to the left side is more than triple that of the right. The magnitude of the dose in the head region was at the low end of the dynamic range of the XR-QA film and the resulting uncertainties were large. To decrease uncertainty in the measurement the scan protocol was run five times on each of the three sets of measurement films. This higher measured dose had less uncertainty. The single scan dose reported was scaled to 1/5 of the measured dose, and the uncertainty calculated from the scaled dose.

4.1.3 Dose Profiles

The dose profiles within the patient from clinical scan protocols in three regions were measured in the left-right (LAT) and anterior-posterior (VERT) orientations. The profile films were placed between the physical slices of the phantom which are labelled in sequence, as presented in table 4.3.

Table 4.3: Position of vertical and lateral profile films within Rando phantom.

Region	Slice	Orientation
Pelvis	29-30	Lateral
	30-31	Vertical
Thorax	15-16	Lateral
	16-17	Vertical
Head and Neck	4-5	Vertical
	5-6	Lateral

4.1.2.3 Head and Neck Region

The obtained dose profiles through the Rando phantom using the Head and Neck CBCT scan protocol are presented in figure 4.7 (vertical dose profile) and in figure 4.8 (lateral dose profile).

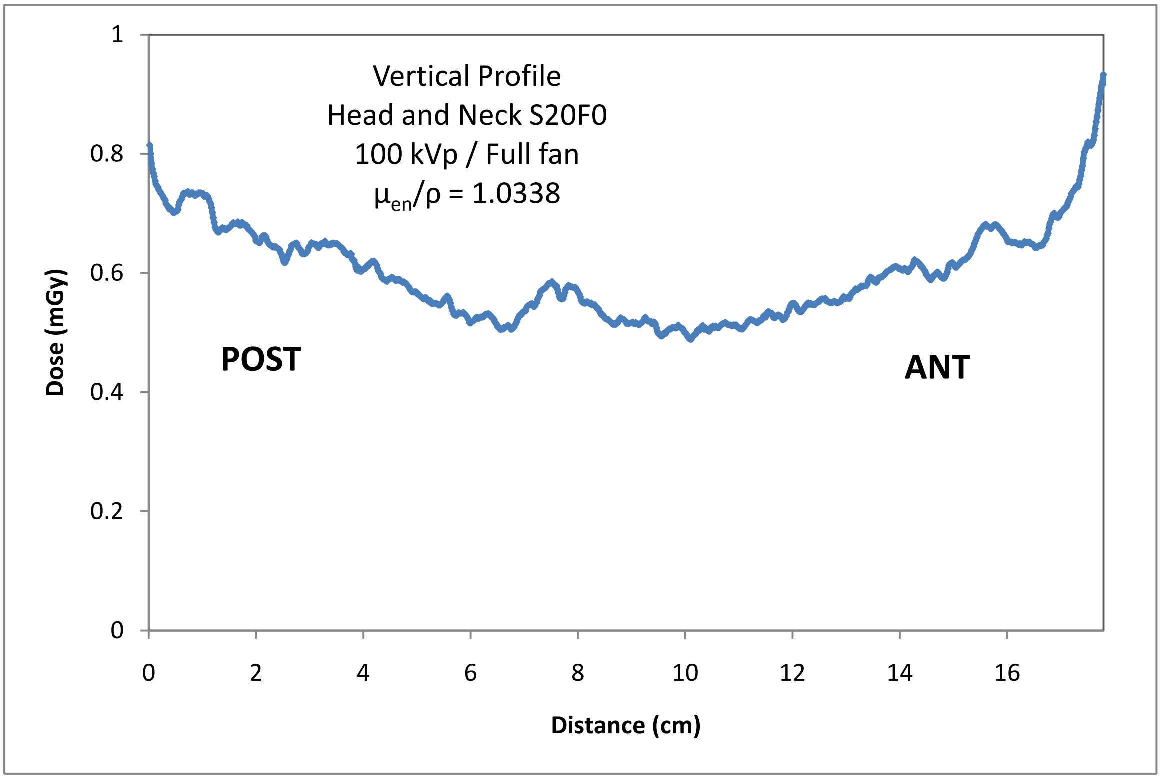

Figure 4.7: Vertical dose profile through the Rando phantom in the head and neck region during the clinical CBCT scan using the Head and Neck protocol.

As one can see in figure 4.7, the dose during the Head and Neck CBCT scan in the anterior and posterior aspects are roughly equivalent resulting from the symmetry about the left aspect. The small difference in dose between the ANT and POST aspects is a result of attenuation of the imaging beam through the treatment table.

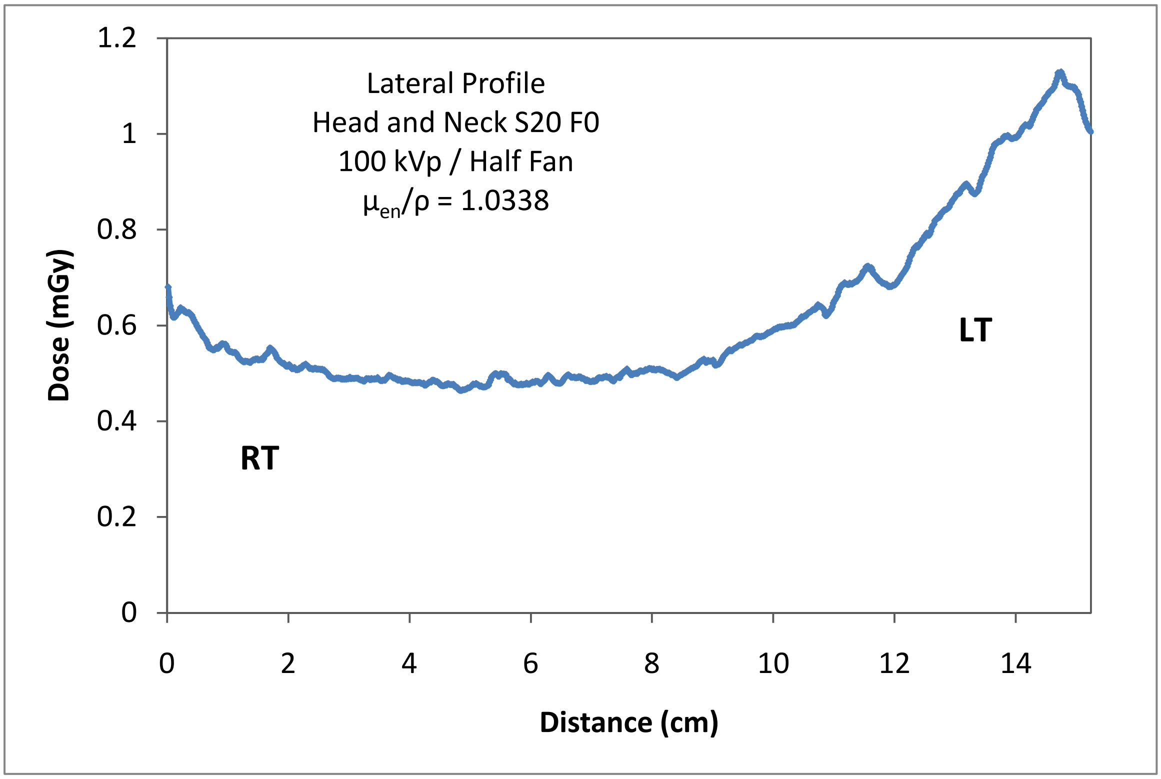

Figure 4.8: Lateral dose profile through the Rando phantom in the head and neck region during the clinical CBCT scan using the Head and Neck protocol.

The lateral dose profile during the Head and Neck CBCT scan exhibits the asymmetry between the left and right aspect of the gantry sweep for this protocol. The low tube output used for this protocol of 36.1 mAs results in a low given dose. It is to note that the dose profiles do not match the skin doses from table 4.2 as the profile films were not intended to measure skin dose. Cutting of the profile films and misalignment of film-edge with phantom surface prevent accurate skin dose measurement with profile films, and so the ends of the film were taken out of the measured data.

4.1.2.4 Thorax Region

Figure 4.9 presents the vertical dose profile obtained using the Chest CBCT protocol. The higher mAs from this scan results in higher deposited dose. The lateral dose profile obtained from the same CBCT scanning protocol is presented in figure 4.10

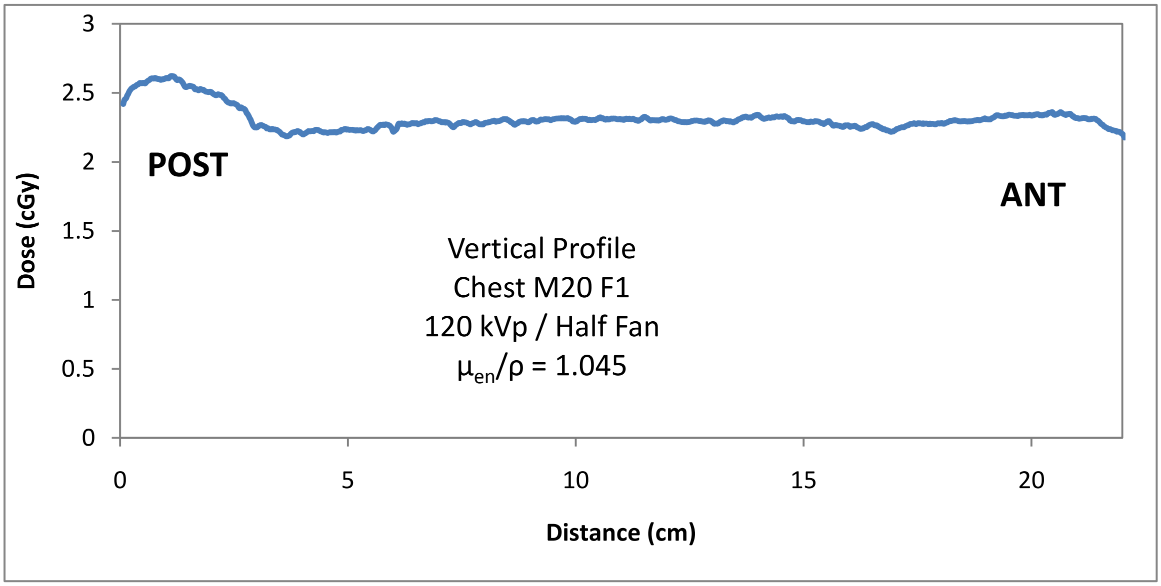

Figure 4.9: Vertical dose profile through the Rando phantom in the thorax region during the clinical CBCT scan obtained using the Chest CBCT protocol.

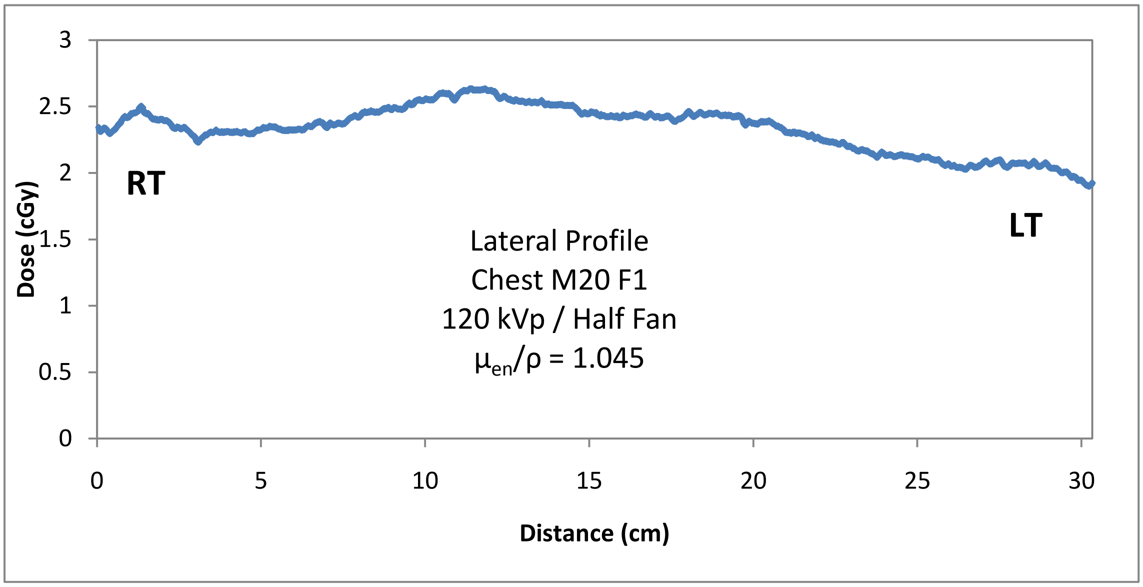

Figure 4.10: Lateral dose profile through the Rando phantom in the thorax region during the clinical CBCT scan obtained using the Chest CBCT protocol.

4.1.2.5 Pelvic Region

The obtained dose profiles for pelvic region using the Prostate CBCT protocol are presented in figures 4.11 (vertical) and 4.12 (lateral).

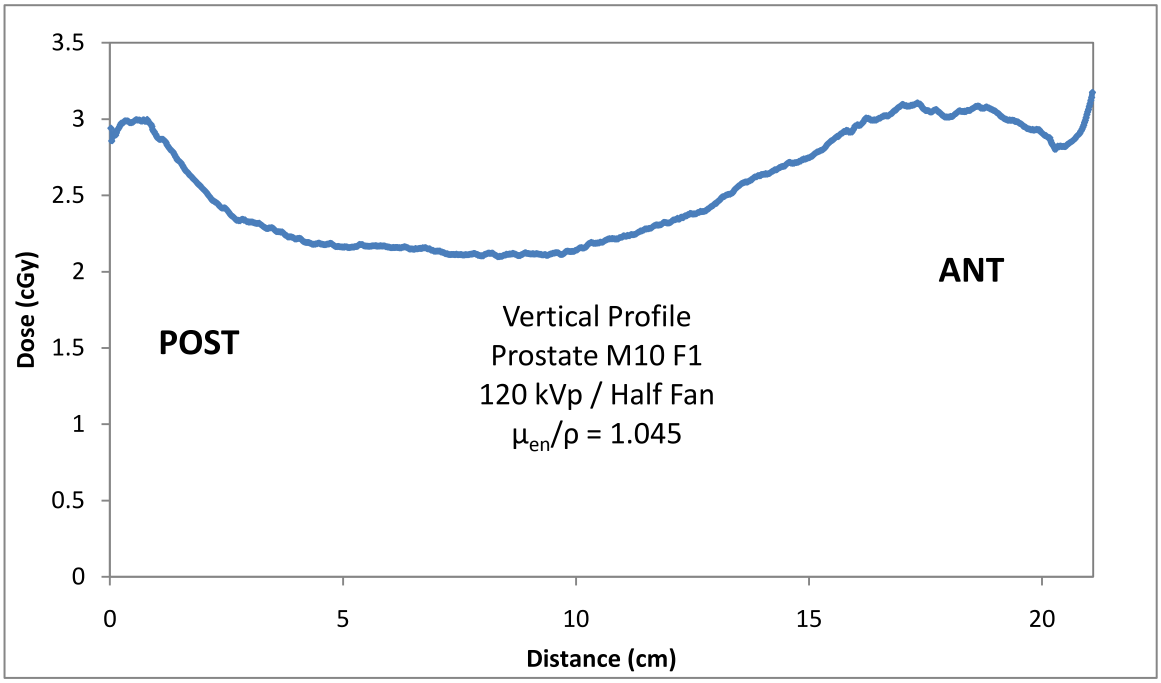

Figure 4.11: Vertical dose profile through Rando phantom in the pelvic region during clinical CBCT scan obtained using Prostate CBCT protocol.

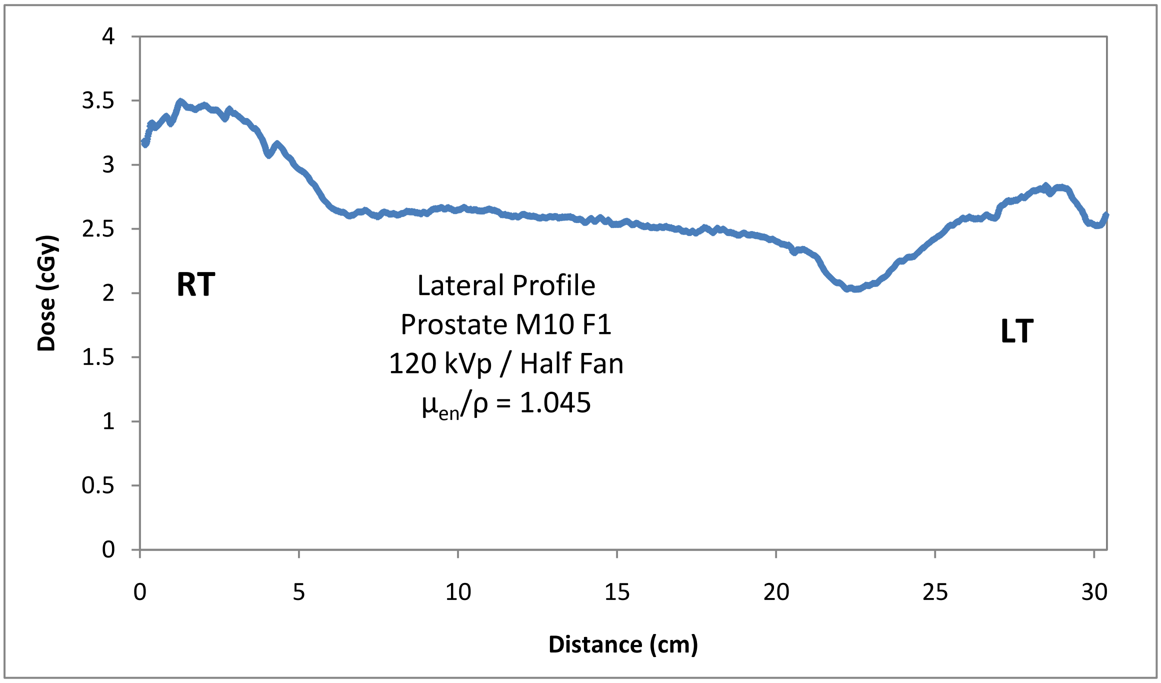

Figure 4.12: Lateral dose profile through the Rando phantom in the pelvic region during the clinical CBCT scan obtained using the Prostate CBCT protocol.

In conclusion, the effect of mAs on dose is clearly illustrated by the results of both the skin and profile dose measurements. The asymmetry of the head and neck protocol gantry sweep parameter lead to an asymmetry in the deposited dose to the patient. One feature unique to the XVI system is the ability to customize the protocol parameters. By changing the mA, ms, and number of frames acquired one could modulate the dose to the patient for a given beam quality. Additionally, customization of the gantry sweep parameter for head and neck protocols could allow one to place the higher dose from the asymmetry at the posterior of the patient, away from the lenses of the eyes, or to alternate daily between clockwise and counter-clockwise rotation to evenly distribute dose across the course of treatment.

4.2 CBCT Based Dose Calculations

The results of dose calculation in Pinnacle are given in this section, and the CT-D curves generated for heterogeneity correction are presented.

4.2.1 CT-D Curves

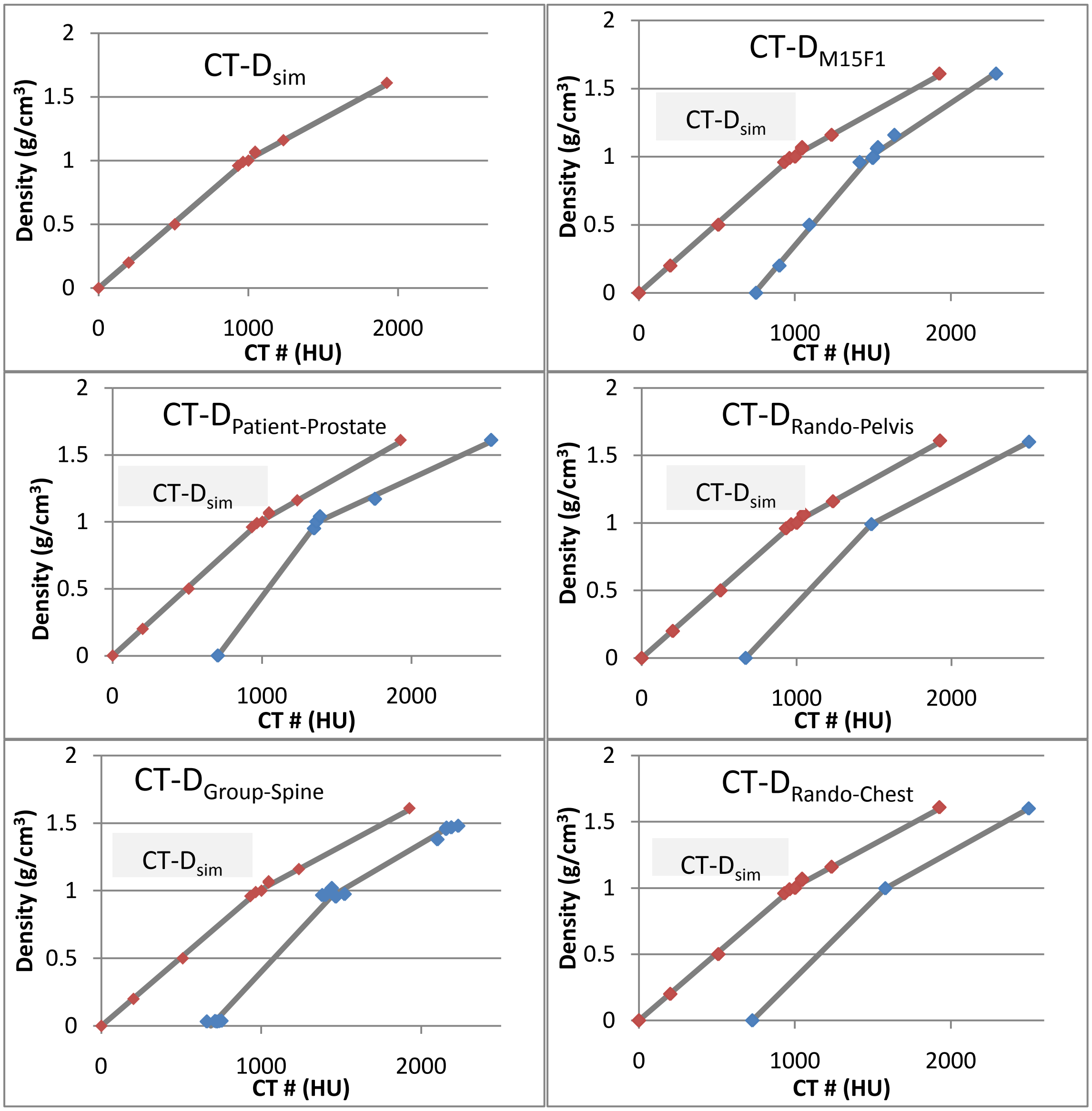

Figure 4.13: Different CT-D curves for heterogeneity corrected dose calculations in Pinnacle. Extended range of densities used in the TPS has been left out to better illustrate the measured data.

A total of six density curves were created for Hounsfield unit to density calibration in the Pinnacle TPS. The HU and density points were plotted and fitted with a bilinear function in TableCurve. The Pinnacle TPS requires that the first point be at the origin. Additionally, Phillips does not recommend a fit-curve for use in the CT-D calibration; instead the system automatically interpolates between plotted points in the CT-D data table. Rather than adhere to these recommendations the zero density y-axis intercept was kept true to the measured data by plotting the first point at the origin and the next at the measured zero density HU point. Then the calculated fit-curve was imported by placing three points in the table for densities of 0 g/cm^3, 1 g/cm^3, and a third at 5 g/cm^3. Each point was calculated from the bilinear fit-function ($R^2 > 0.99$) so as to make the interpolation in Pinnacle match the desired fit function. The third density did not come from measured data in any image set, but came from an interpolation of the highest density point of the fit-function for the purpose of extending the range of the CT-D curve to account for high density objects which might be present in some patients (e.g. seeds, titanium hardware).

CT-D$_{sim}$ and CT-D$_{M15F1}$ were created from the same density phantom and so share the same density points, which came from the manufacturer's product information. The density from the Rando and patient based curves came from CT scans. In keeping with the literature the density points for the group based curves were restricted to air, water, and bone for creation of the CT-D curve. For the prostate patient based curve more points were used where reasonable. The density points for the Rando phantom were limited by the number of different materials present, which fit with the three point model in use for the group based approach. For the group based approach a total of five patients were used and the air, water, and bone data points were plotted and a fit function found from them for the CT-D curve. No water exists in the thorax as it does in the pelvis region in the bladder so soft tissue with density close to unity was used as a surrogate and the intersection of the bilinear function placed here. Dense bone was not used in the group based spine due to the lack of large volumes of it present in the vertebrae, and instead the less dense region in the interior of the vertebral body was used, and the higher densities interpolated.

4.2.2 Prostate Patient

Dose to volumes of interest in a prostate patient was calculated in Pinnacle on CT simulator images and CBCT daily IGRT images for a 7 field step-and-shoot IMRT plan with segments, beam angles, and monitor units held constant. Three CT-D curves were used for heterogeneity corrections: CT-D_{sim}, CT-D_{M15F1}, and CT-$D_{\text{Paitent-Prostate}}$. The CBCT images for this patient were acquired with the same imaging geometry (M15F1) as the scan of the density phantom for the creation of CT-D_{M15F1}. The dose from one fraction was calculated in the original treatment plan on the CT image set for the patient and the resulting DVH plotted. The DVH from one fraction in the CBCT image set for each of the three CT-D curves was plotted over the original treatment planning DVH for comparison, the results of which are presented in figures 4.14-4.16.

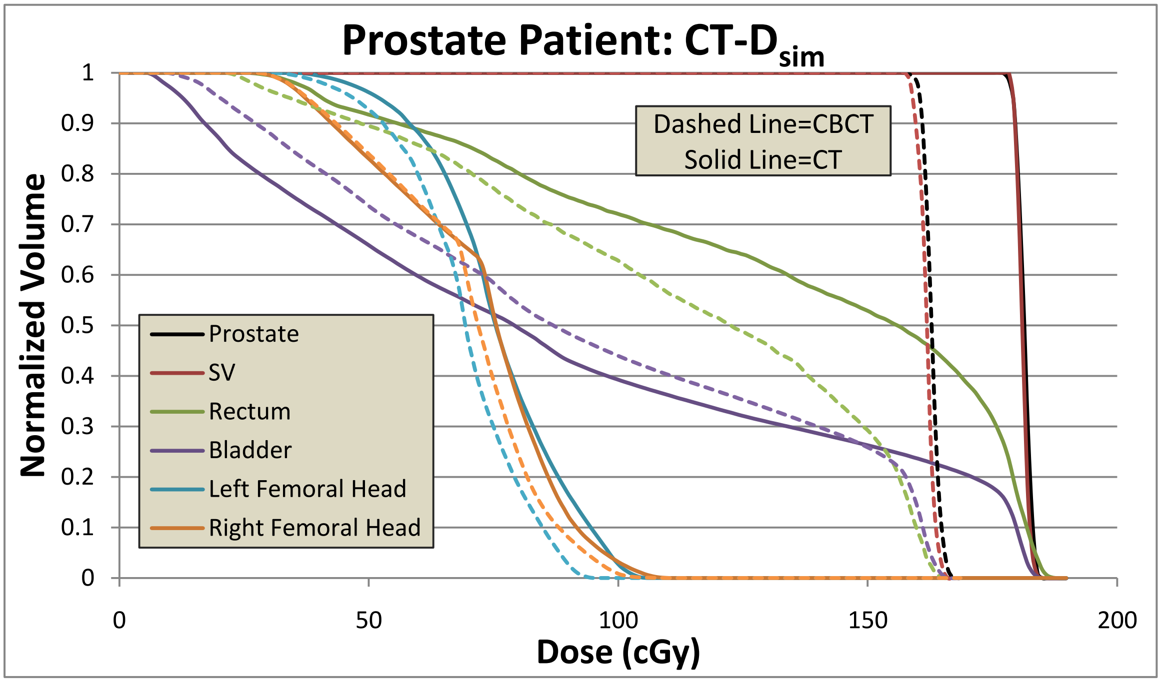

Figure 4.14: DVH results of CBCT: CT-D_{sim} vs. planning CT.

The DVH results for the CT-D_{sim} density curve show a gross underestimate of dose for the prostate and seminal vesicles, and a small underestimation for the femoral heads (figure 4.14). The slope of the curve for the prostate and seminal vesicles indicates a good agreement in the amount of uniformity of dose in the plan. The CBCT calculated dose for the critical structures surrounding the prostate (bladder and rectum) is in poor agreement with the original planning CT and leads to higher actual dose to the rectum at all volumes and a higher actual dose to the bladder for normalized volumes of 0.25 and less.

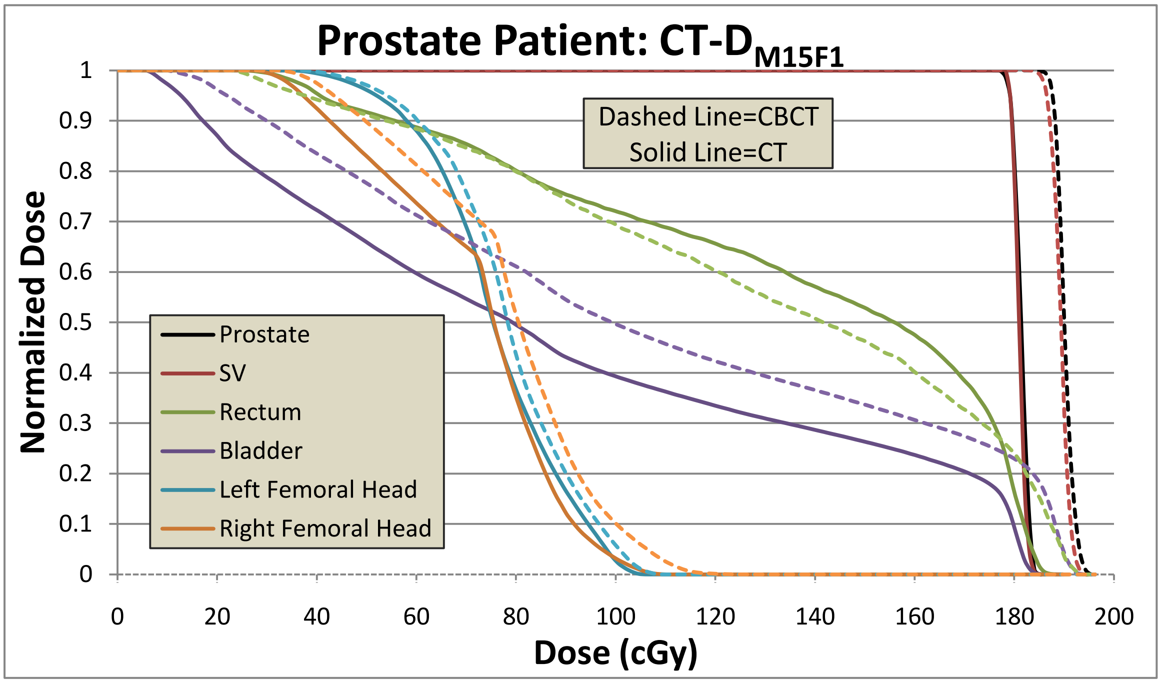

Figure 4.15: DVH results of CBCT: CT-D_{M15F1} vs. planning CT

With the density phantom based correction of CT-D_{M15F1} the DVH curves for the prostate and seminal vesicles move closer together, as do the bladder, rectum, and femoral heads (figure 4.15). The CBCT based dose calculation overestimates the dose to the target structures, while the uniformity is unchanged. The agreement of the bladder and rectum doses is closer with this correction. With the density phantom based correction, the estimation of the dose to the bladder changed from an underestimation at high doses-low volumes to a general overestimation for the entire range.

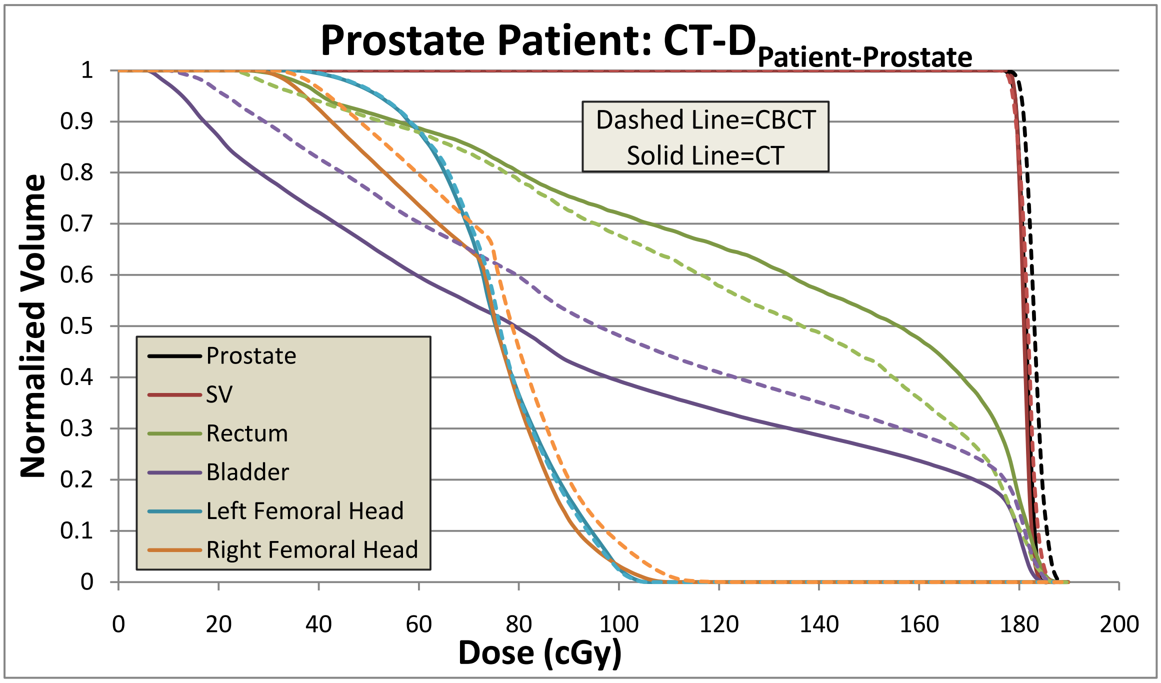

Figure 4.16: DVH results of CBCT: CT-D$_{Patient-Prostate}$ vs. planning CT.

With the application of the patient based density curve CT-D$_{Patient-Prostate}$ the DVH for the prostate and seminal vesicles is within close visual agreement (figure 4.16). The DVH for the femoral heads is in closer agreement than with the phantom based or simulator density curves. The CBCT based dose to the prostate is still overestimated though now by a much smaller amount. Table 4.4 gives the mean dose to each structure for the three CBCT calculations and the CT based calculation.

Table 4.4: Prostate patient; mean dose to ROI for each image set / density curve.

Image Set	Density Curve	ROI	Mean Dose (cGy)	% Difference (vs. Planning CT)
Planning CT	CT-D_{sim}	Prostate	182.3	NA
		SV	182.1	NA
		Bladder	91.6	NA
		Rectum	135.7	NA
		Lt Fem Head	76.8	NA
		Rt Fem Head	72.4	NA
CBCT	CT-D_{sim}	Prostate	163.7	-10.2%
		SV	162.7	-10.7%
		Bladder	95.2	3.9%
		Rectum	113.9	-16.1%
		Lt Fem Head	69.8	-9.1%
		Rt Fem Head	70.1	-3.2%
CBCT	CT-D_{M15F1}	Prostate	191.2	4.9%
		SV	190.3	4.5%
		Bladder	109.4	19.4%
		Rectum	131.8	-2.9%
		Lt Fem Head	79.4	3.4%
		Rt Fem Head	79.2	9.4%
CBCT	CT-$D_{Prostate\text{-}Patient}$	Prostate	184.1	1.0%
		SV	182.6	0.3%
		Bladder	105.7	15.4%
		Rectum	127.3	-6.2%
		Lt Fem Head	77	0.3%
		Rt Fem Head	77.1	6.5%

The mean dose difference in the prostate and seminal vesicles in the uncorrected CBCT image set with density curve CT-D_{sim} are -10.2% and -10.7%

when compared to the planning CT calculated dose. This improves to +4.9% and +4.5% with application of the scan protocol-specific density phantom based CT-D_{M15F1}. The patient based density curve CT-$D_{Patient\text{-}Prostate}$ improves the dose agreement to +1.0% and +0.3% for the prostate and seminal vesicles respectively. For all three cases the rectum and bladder doses are in poor agreement; ranging from -2.9% up to +19.4% when compared with the planning CT. This amount of error in dose calculation is in disagreement with the target structures whose maximum dose difference was -10.7% for the seminal vesicles calculated with CT-D_{sim}. Two possible explanations exist for this discrepancy: The dose calculated in the non-uniform dose region outside of the PTV experiences higher error due to density correction effects on the scatter contribution outside of the primary beam, or that different bladder and rectum filling between the simulation image and the daily IGRT image have changed the volume of the structures and their position relative to the treatment beam. To reduce the error due to changes in anatomy, this process was repeated on the anthropomorphic Rando phantom.

4.2.3 Rando Phantom-Pelvis

The anthropomorphic Rando phantom provides an ideal setup to further analyze the accuracy of dose calculation in CBCT image sets. The solid construction of the phantom makes it possible to eliminate any change in internal anatomy as well as reduce setup errors between CT and CBCT image acquisitions. The femoral heads within the pelvis region of the phantom were contoured, and simulated prostate, bladder, and rectum ROI were placed within the CT and CBCT image sets, registered to bony anatomy and external contour. A seven beam IMRT plan was created for the CT image and the dose from the beams calculated for the CT image set and for the CBCT image set using the three CT-D curves. The DVH for each of the three CBCT CT-D curves were calculated and graphed against the planning CT DVH. The obtained results are presented in figures 4.17, 4.18, and 4.19. The difference between those methods and the planning CT results are presented in table 4.5

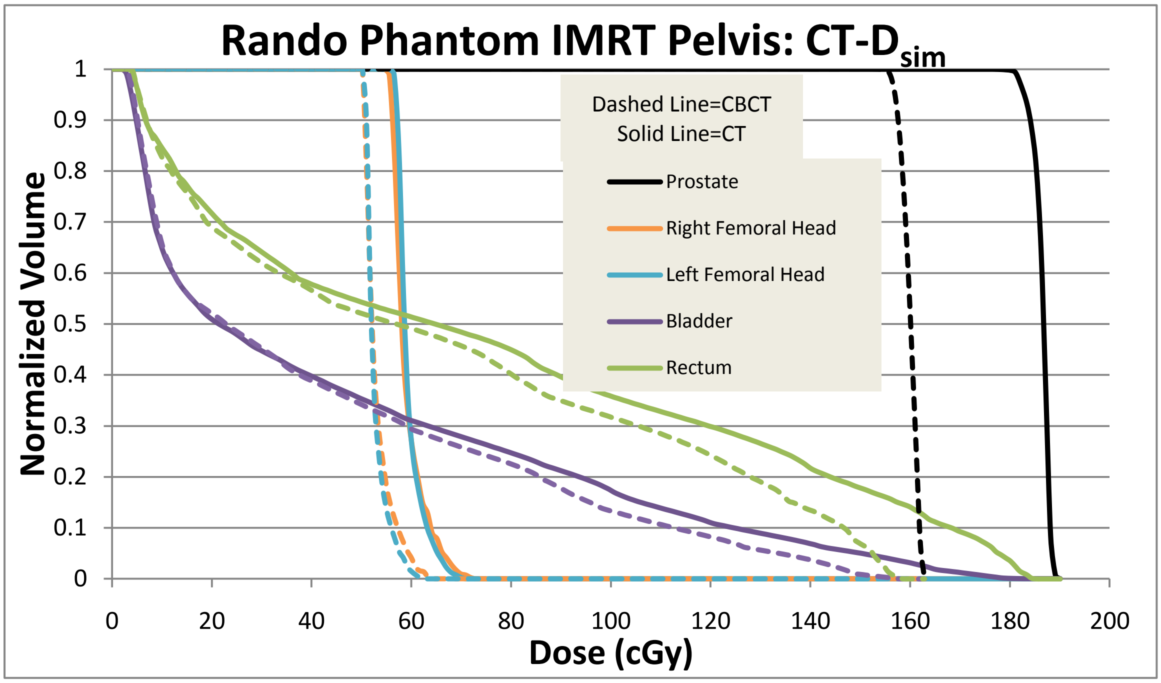

Figure 4.17: Rando Prostate DVH results of CBCT: CT-D_{sim} vs. planning CT.

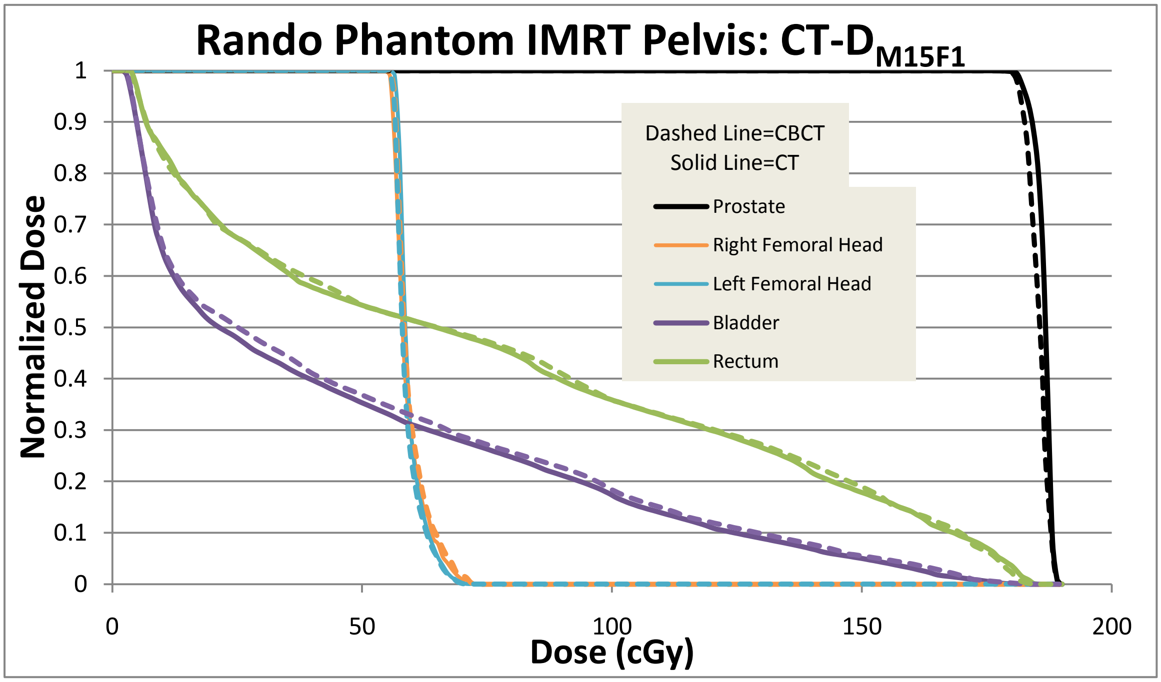

Figure 4.18: Rando Prostate DVH results of CBCT: CT-$D_{M15F1\ vs}$. planning CT.

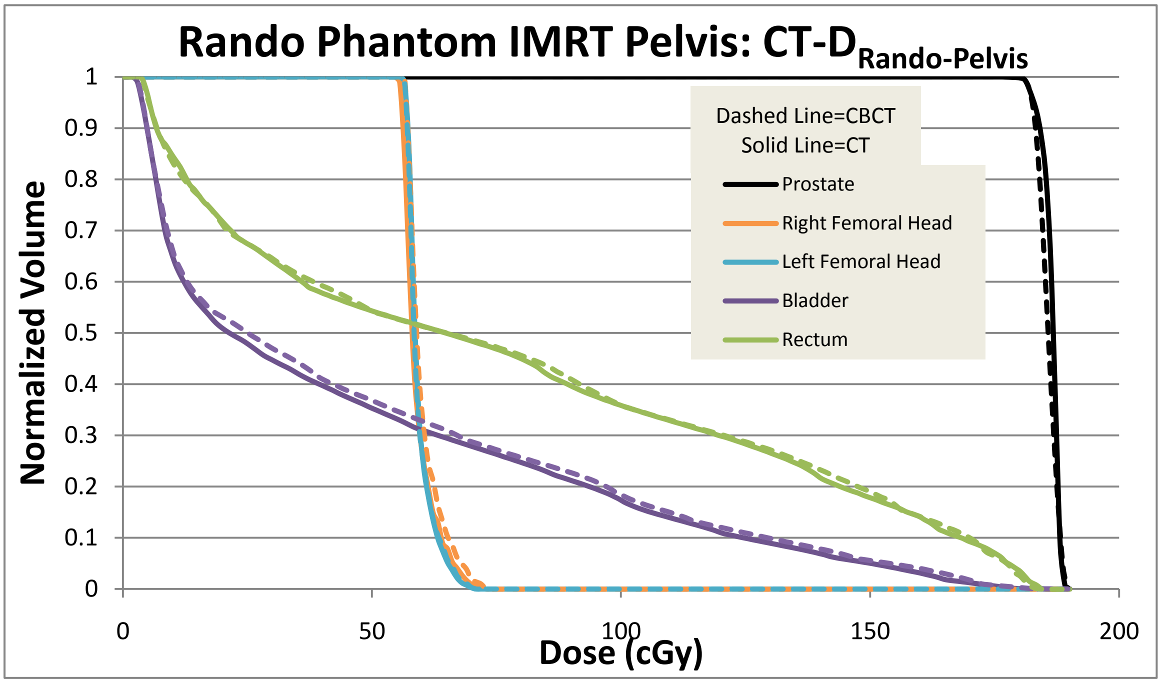

Figure 4.19: Rando Prostate DVH results of CBCT: CT-D$_{Rando-Pelvis}$ vs. planning CT.

Use of CT-D$_{sim}$ results in a large underestimation of dose to the target volume, as seen with the patient based results (figure 4.17). Use of CT-D$_{M15F1}$ improves the results significantly over the uncorrected calculations (figure 4.18). Application of CT-D$_{Rando-Pelvis}$ makes no visible improvement over the density phantom based correction (figure 4.19). The agreement between CT-D$_{M15F1}$ and CT-D$_{Rando-Pelvis}$ calculated results is due to the similarity in axial size and shape of the density and Rando phantom.

Table 4.5: Rando prostate; mean dose to ROI for each image set / density curve.

Image Set	Density Table	ROI	Mean Dose (cGy)	% Difference (vs. Planning CT)
Planning CT	CT-D_{sim}	Prostate	187.3	NA
		Bladder	47.1	NA
		Rectum	77	NA
		Lt Femoral Head	60.6	NA
		Rt Femoral Head	60.2	NA
CBCT	CT-D_{sim}	Prostate	160.8	-14.1%
		Bladder	43.5	-7.6%
		Rectum	67.7	-12.1%
		Lt Femoral Head	53.6	-11.6%
		Rt Femoral Head	53.9	-10.5%
CBCT	CT-D_{M15F1}	Prostate	186.1	-0.6%
		Bladder	49	4.0%
		Rectum	77.5	0.6%
		Lt Femoral Head	59.9	-1.2%
		Rt Femoral Head	60.6	0.7%
CBCT	CT-$D_{Rando\text{-}Pelvis}$	Prostate	186.7	-0.3%
		Bladder	49	4.0%
		Rectum	77.5	0.6%
		Lt Femoral Head	60.4	-0.3%
		Rt Femoral Head	61.1	1.5%

The DVH for CT-D_{M15F1} and CT-$D_{Rando\text{-}Pelvis}$ are nearly identical for all ROI, and in good agreement with the results from the planning CT. The percent difference in mean dose to the prostate calculated from both of these density curves compared to the panning CT is less than 1%. The mean dose to the bladder for each of these is 4% higher than the planning CT. Because the agreement with planning CT for the prostate is on the same order as was seen in the patient case, and with the reduction of error due to changes in anatomy when using the solid phantom, it can be conjectured that the remaining error above what is seen in the prostate (<1%) is due to effects on the calculated dose distribution in the scatter and low dose regions generating from the heterogeneity corrections based on the CT-D curve. To investigate this possibility a gamma analysis on the absolute dose distribution was performed in the axial plane passing through the isocenter. The planar dose from the CBCT data set calculated with CT-$D_{\text{Rando-Pelvis}}$, and the planar dose from the planning CT data set were imported into the MapCheck2 (Sun Nuclear Corporation, Melbourne, FL) software for gamma analysis. Strict parameters of 0.5% dose difference and 0.5 mm distance to agreement were used in order to view the results of the most points for this purpose.

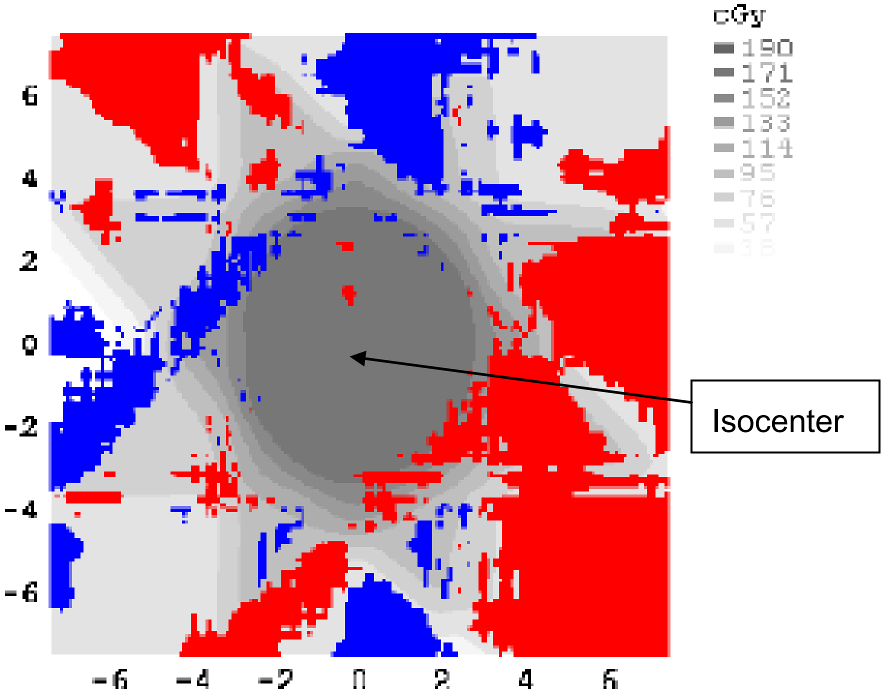

Figure 4.20: Gamma analysis results for a 15 x 15 cm^2 grid centered on the isocenter. The red and blue pixels indicate hot and cold failing points.

The gamma analysis was performed for a 15 x 15 cm^2 grid centered on the isocenter in the axial plane. The high dose region in the middle surrounds the target prostate. Of the 22,201 points analyzed 60% passed this strict gamma analysis, the overwhelming majority of which lie outside the high dose region. The bladder and prostate being in this region, it can be concluded that the residual error in the calculated dose for these structures can be in part attributed to this low dose region phenomenon. Some anatomical error still exists despite the use of the Rando phantom however, due to the use of contouring in the treatment planning system for these structures. The original contours from the

CT image set were saved as mesh structures and imported into the CBCT data set. The mesh structures have limited vertices which limit the reproducibility, and the positioning of the contours on the CBCT image cannot be completely matched to the original CT image. It may be assumed that some error still remains from this process, which combined with the dose calculation error outside the high dose region is responsible for the remaining error seen in the DVH.

4.2.4 Spine Patients

An immediately beneficial application of CBCT for planning purposes is the emergency spine case. Emergency spine patients are CT simulated, planned, and treated immediately afterward, and receive palliative treatments of fewer fractions than a typical curative case. If the patient could be simulated on the treatment table with the integrated CBCT system it would reduce the pain and discomfort from moving between simulator table and treatment table, reduce workload on the simulator, and possibly decrease the total treatment time. To evaluate the accuracy of dose calculations from CBCT image sets in the thorax region for spine treatments, two CT-D curves were created. The first was the CT-D_{M15F1} used previously, the second a patient based curve (CT-$D_{Group\text{-}Spine}$)

generated from density and HU points collected from 5 patients and fit in TableCurve.

The image sets of two patients were used for analysis: A 93 kg male, and a 48 kg female. As opposed to the prostate case, the treatment plan for each of these patients was created using the CBCT image set and the comparison done by transferring that plan onto the CT image set. The plan was a simple two beam AP-PA setup using a wedged AP field, with the goal of giving a therapeutic dose to the affected vertebrae (simulated) and one vertebrae superior and inferior. The primary dosimetric aspect of concern to the physician for palliative emergency spine cases at this clinic is the isodose distribution. The analysis was therefore done by comparing between the CT and CBCT image sets:

1. The isodose line which covers the target vertebrae.
2. The highest isodose line which touches the spinal cord.

For each patient there were 6 plans created: 2 photon energies (6 MV and 15 MV) with dose calculated from 3 CT-D curves ($\text{CT-D}_{\text{Group-Spine}}$, $\text{CT-D}_{\text{M15F1}}$, and CT-D_{sim}). The MU from each CBCT plan was transferred to the CT image set and the dose was calculated using the planning CT-D_{sim}. Table 4.6 summarizes the results and gives the difference in target coverage and max cord dose between the CBCT and CT dose calculations for each plan.

Table 4.6: Results of CBCT vs. CT dose calculations for emergency spine cases.

Patient	CT-D	Energy	Image Set	Coverage	% Difference	Cord Dose	% Difference
Male	CT-D_{sim}	6 MV	CBCT	450	**-10.9%**	540	**-8.5%**
			CT	505		590	
		15 MV	CBCT	450	**-7.2%**	515	**-6.4%**
			CT	485		550	
	CT-D_{M15F1}	6 MV	CBCT	450	**-2.2%**	525	**-1.9%**
			CT	460		535	
		15 MV	CBCT	450	**0.0%**	510	**0.0%**
			CT	450		510	
	CT-$D_{Group\text{-}Spine}$	6 MV	CBCT	450	**0.0%**	525	**-0.9%**
			CT	450		530	
		15 MV	CBCT	450	**0.0%**	510	**-1.0%**
			CT	450		515	
Female	CT-D_{sim}	6 MV	CBCT	450	**-6.3%**	525	**-4.5%**
			CT	480		550	
		15 MV	CBCT	450	**-4.3%**	510	**-2.9%**
			CT	470		525	
	CT-D_{M15F1}	6 MV	CBCT	450	**0.0%**	520	**1.0%**
			CT	450		515	
		15 MV	CBCT	450	**0.0%**	500	**0.0%**
			CT	450		500	
	CT-$D_{Group\text{-}Spine}$	6 MV	CBCT	450	**2.3%**	510	**0.0%**
			CT	440		510	
		15 MV	CBCT	450	**0.0%**	500	**0.0%**
			CT	450		500	
Rando	CT-D_{sim}	6 MV	CBCT	450	**-8.2%**	510	**-8.9%**
			CT	490		560	
		15 MV	CBCT	450	**-6.3%**	500	**-5.7%**
			CT	480		530	
	CT-D_{M15F1}	6 MV	CBCT	450	**-2.2%**	510	**-3.8%**
			CT	460		530	
		15 MV	CBCT	450	**-2.2%**	500	**-2.0%**
			CT	460		510	
	CT-$D_{Rando\text{-}Thorax}$	6 MV	CBCT	450	**1.1%**	500	**-2.0%**
			CT	445		510	
		15 MV	CBCT	450	**0.0%**	490	**0.0%**
			CT	450		490	

Use of CT-D_{sim} lead to a maximum error of -10.9% in calculated dose coverage of the target for the 6 MV male patient plan. The error decreased slightly in the female and Rando plans. Use of CT-D_{M15F1} improved dose calculation for all three cases with a maximum error of -3.8% for the 6 MV Rando plan. For the male and female patients the error when using CT-D_{M15F1} was less than 3% for all plans. Application of CT-$D_{Group\text{-}Spine}$ lead to dose calculations within 1% for the male patient and 3% for the female patient. For all three density curves, use of 15 MV photons improved dose agreement between CBCT and CT image sets in agreement with findings in the literature.[3] Density corrections based on TMR or TAR such as the Modified Batho method yield smaller corrections for higher energies due to the flatter TMR curve for higher energies at depth. Thus the agreement for the 15 MV plans is closer than for 6 MV plans.

References for chapter 4:

1. From a private conversation with Dr. Slobodan Devic, SMDB Jewish General Hospital, December 12, 2009.
2. Song, W. Y.; Kamath, S.; Ozawal, S.; Al Ani, S.; Chvetsov, A.; Lhandare, N.; Palta, J.R.; Liu, C.; Li, J.G.; A dose comparison study between XVI and OBI CBCT systems. *Med. Phys*. 35, 480-486 (2008).
3. Yoo, S.; Yin, F.F.; Dosimetric Feasibiltiy of Cone-beam CT-based Treatement planning compared to ct-based treatment planning. *Int J Radiat Oncol Biol Phys* **66**: 1553-1561, 2006

Chapter 5: Conclusion and Future Work

Conclusion 1:

A 2D reference radiochromic film dosimetry protocol based upon TG-61 formalism employing GAFCHROMIC^{TM} XR-QA model film can be used to accurately measure dose from the Elekta XVI system with low uncertainty. The resulting dose from the XVI CBCT scans of the thorax and pelvis regions reported are on the order of that from typical MV portal images. The scan dose from the head and neck protocol is significantly lower than MV portal imaging and is not a significant contribution to patient dose over the course of external beam radiotherapy. The doses from thorax and pelvis scans on the other hand are high enough to require careful consideration when prescribing frequency of CBCT IGRT. In particular, the skin dose from these scans necessitates close monitoring of the patient for skin effects, as the total skin dose from CBCT IGRT over the course of a treatment can reach 1 Gy or more.

The gantry sweep during scan acquisition plays an important role in the dose distribution from the kV x-rays. The ability to customize the protocol parameters in the XVI system makes it possible to adjust the gantry sweep to place the higher dose regions away from sensitive structures. Additionally, it is possible to reduce the total mAs for a given scan, thereby reducing dose to the patient. This is particularly useful for creating lower mAs protocols for small patients, where the large exit dose from each beam angle increases the total deposited dose significantly. Future work will include an investigation into the reduction of mAs for clinical scan protocols and its effect upon image quality.

Conclusion 2:

XVI CBCT image sets can be used to calculate dose with acceptable accuracy in the Pinnacle treatment planning system. The agreement between CT and CBCT based dose calculation can be improved through the implementation of CT-D curves based upon density phantoms and patient CT image sets. The use of a patient specific CT-D for the prostate patient illustrated the ability of CBCT images to calculate dose and provide an avenue for dose tracking. The accuracy of CBCT based dose calculation for planning a spine treatment is within 1% agreement with CT based calculations. The agreement increases for higher beam energies. Though in this study the CT-D based method for scatter correction exhibits reasonably close agreement to the standard fan beam CT, more work is necessary before use of CBCT images for treatment planning can be considered in clinical practice. Dose tracking with CBCT images on the other hand, without the need for the level of accuracy required for treatment planning, could immediately find use in the clinic.